# Supporting Information: Surface Reaction Barriometry: Methane Dissociation on Flat and Stepped Transition Metal Surfaces

*Davide Migliorini[1‡], Helen Chadwick[2‡†], Francesco Nattino[1], Ana Gutiérrez-González[2], Eric Dombrowski[3], Eric A. High[3], Han Guo[4], Arthur L. Utz[3], Bret Jackson[4], Rainer D. Beck[2*], Geert-Jan Kroes[1*]*

[1]Leiden Institute of Chemistry, Gorlaeus Laboratories, Leiden University, P.O. Box 9502, 2300 RA Leiden, The Netherlands.

[2]Laboratoire de Chimie Physique Moléculaire, Ecole Polytechnique Fédérale de Lausanne, CH-1015 Lausanne, Switzerland.

[3]Department of Chemistry and W. M. Keck Foundation Laboratory for Materials Chemistry Tufts University, Medford, MA 02155, USA.

[4]Department of Chemistry, University of Massachusetts, Amherst, Massachusetts 01003, USA.

Correspondence to *g.j.kroes@chem.leidenuniv.nl , *rainer.beck@epfl.ch

[‡]These authors have contributed equally to this work.

[†]Present address: Leiden Institute of Chemistry, Gorlaeus Laboratories, Leiden University, P.O. Box 9502, 2300 RA Leiden, The Netherlands.

## 1. Experimental Methods

### 1.1 General approach

The dissociation experiments for $CHD_3$ on Ni(111) were done at Tufts University[1] and the experiments on the platinum surfaces at the EPFL[2–10]. The experimental methods employed for the Ni(111) measurements have been published previously[11] and we will not reproduce that information here. The molecular beam/surface science machine at the EPFL[7] consists of a triply differentially pumped molecular beam source chamber attached to an ultrahigh vacuum (UHV) chamber, with a base pressure of $5x10^{-11}$ mbar. A continuous molecular beam was produced by expanding a 1.5% $CHD_3$ in $H_2$ mixture through a nozzle held at constant temperature in the range of 298 K to 650 K. This created molecules with a well-defined incident translational energy ($\langle E_i \rangle$) between 58 kJ/mol and 120 kJ/mol (see Table S2). The $CHD_3$ collided with the Pt(111) or Pt(211) surface, held at 500 K or 650 K respectively, at incidence normal to the surface.

The initial sticking coefficients ($S_0$) for the dissociative chemisorption of $CHD_3$ on Pt(111) and Pt(211) were measured using the King and Wells (K&W) beam reflectivity technique[3,12]. We first measured the laser-off reactivity ($S_0^{off}$) for a range of $\langle E_i \rangle$, which was achieved by varying the nozzle temperature ($T_n$). This also changed the rotational and vibrational state populations in the molecular beam. Whilst rotational cooling is efficient in the supersonic expansion ($T_{rot} \approx 10$ to 40 K), vibrational cooling is inefficient with $T_{vib}$ taken to be the same as $T_n$. The measured $S_0^{off}$ reflect the vibrationally averaged reactivity at each incident kinetic energy.

We measured the quantum state resolved reactivity for $CHD_3$ molecules prepared with a single quantum of CH stretch vibration ($\nu_1$) on Pt(111) and Pt(211). Infrared laser pumping was used to excite the incident $CHD_3$ from $v$=0, $J$=1 and $K$=1 to $\nu_1$=1, $J$=2 and $K$=1 by rapid adiabatic passage (RAP) [13]. As a number of rotational and vibrational states are populated in the incident

beam, the infrared pumping prepares only a fraction ($f_{\mathrm{exc}}$) of the incident $CHD_3$ in the selected rovibrational state. Therefore, the state resolved reactivity $S_0^{\nu_1=1}$ ($\nu_1$=1, *J*=2 and *K*=1) is obtained from the difference of the two averaged measurements $S_0^{on}$ and $S_0^{off}$, with and without infrared pumping as described in Sec. 1.5.2.

Further specific details about the experimental methods, results, and data analysis for both the Pt(111) and Pt(211) measurements can be found in the sections below.

## 1.2 Molecular beam and surface preparation

Sticking coefficients were measured using $CHD_3$ (Cambridge Isotope Laboratory, 99% isotopic purity, 98% chemical purity) diluted to 1.5% concentration in $H_2$ (99.9999%). The 1.5% $CHD_3$ in $H_2$ mix was further purified by a Supelpure oxygen/moisture trap in the gas line before reaching the nozzle. The molecular beam was formed by expanding the gas mixture through a stainless steel nozzle with a 50 μm diameter hole, using backing pressures of between 1.4 bar and 2 bar. A K-type thermocouple was spot welded to the end of the nozzle to monitor $T_n$ during the measurements. The nozzle was resistively heated to up to 650 K to control the incident translational energy of the molecular beam to minimize the influence of thermal vibrational excitation on the measured sticking coefficients. An SRS PTC10 temperature (PID) controller was used to stabilize $T_n$ to $\pm 0.1$ K.

The Pt(111) surface (Surface Preparation Laboratory), cut to within 0.1° of the (111) plane, was mounted on two tungsten wires attached to a liquid nitrogen cooled bath cryostat[14]. The surface temperature was measured by a K-type thermocouple inserted in a hole cut by spark erosion into the side of the crystal. The Pt(111) sample could be heated to temperatures greater

than 1100 K by passing a DC current through the tungsten wires and cooled through thermal contact with a liquid nitrogen reservoir to 80 K.

The Pt(211) surface (Surface Preparation Laboratory), cut to within 0.1° of the (211) plane was placed in a tantalum holder which was mounted between two tungsten wires in the UHV chamber. A K-type thermocouple was spot-welded to the tantalum holder and used to monitor the temperature of the surface. From temperature programmed desorption (TPD) measurements we estimate there was at most a 10 K difference in temperature between the tantalum holder and the platinum surface. The Pt(211) surface could be resistively heated to over 1100 K, and cooled using liquid nitrogen to 100 K.

During the deposition measurements, the surface temperature ($T_s$) of the Pt(111) crystal was maintained at 500 K, and the Pt(211) crystal at 650 K using an SRS PTC10 temperature (PID) controller. These temperatures were used as they were above the recombinative desorption temperature of $H_2$ and other contaminants (see Sec. 1.6). Between consecutive measurements, the surface was cleaned using argon sputtering at a pressure of $1x10^{-7}$ mbar for 10 minutes, and annealing at 1100 K for 2 minutes. The surface cleanliness was verified by Auger electron spectroscopy.

## 1.3 Molecular beam characterization

In a supersonic expansion, cooling of the translational and rotational degrees of freedom is efficient, whereas vibrational cooling is inefficient. This has consequences for both the experiments and calculations. For the experiments, the extent of vibrational and rotational cooling determines the population of the $v$=0, $J$=1 and $K$=1 state of $CHD_3$ from which the laser excitation takes place and therefore the maximum $f_{\mathrm{exc}}$ which can be prepared by infrared pumping in a

specific rovibrationally excited state. For the calculations, it is important to reproduce the actual experimental parameters such as the distribution of thermally populated vibrational states to allow accurate simulations to be performed. The vibrational state distribution in the molecular beam was modelled using a Boltzmann distribution for a given $T_n$ used in the experiment.

### 1.3.1 Translational energy distribution

The velocity distribution of the molecular beam was determined with time-of-flight (TOF) methods using an on-axis quadrupole mass spectrometer (QMS) (Pfeiffer QMG 421) in conjunction with a fast chopper wheel spinning at 200 Hz. The QMS records the distribution of arrival times of methane in the chopped molecular beam. The measured time-of-flight profiles are fit by a flux weighted Maxwell Boltzmann velocity distribution[15] to obtain the stream velocity ($v_0$) and the width parameter ($\alpha$) which characterizes the spread of velocities in the molecular beam. The fitting method deconvolutes the known chopper function from the measured distribution and accounts for the ion flight time and the delay between the chopper opening and the trigger signal. Table S2 lists the values of $T_n$, $v_0$ and $\alpha$ obtained experimentally, which were used as inputs to the *ab initio* molecular dynamics (AIMD) calculations to ensure the initial velocity distributions of the beams were modelled accurately.

To be able to determine the chopper delay and the ion flight time with sufficient accuracy, the QMS was mounted on a translation stage, and TOF profiles were measured at different chopper to QMS distances (d), as shown in the left hand panel of Fig. S4. For each value of d, the chopper delay and ion flight time do not change, meaning the change in the TOF distribution is only due to Δd. The TOF profiles measured at each d are fit to a flux weighted Maxwell Boltzmann velocity distribution [15] to obtain $t_0$, which can then be plotted against Δd to obtain the velocity, as shown

in the right hand panel of Fig. S4. These measurements were repeated for a range of gases (He, Ne, Ar, 1% $CH_4$ in $H_2$ and 1.5% $CHD_3$ in $H_2$) for several different values of $T_n$ to obtain molecular beam velocities between 600 $ms^{-1}$ and 3500 $ms^{-1}$. From these measurements, we determined the ion flight distance and the chopper delay, as well as the neutral flight distance for a fixed chopper to QMS distance. Once calibrated, this allowed the velocity distribution of the $CHD_3$ in the experiments presented here to be obtained from a single TOF measurement.

### 1.4 Infrared laser excitation of $CHD_3$ in the molecular beam

For the laser-on measurements, $CHD_3$ was prepared with a single quantum of CH stretch ($\nu_1$) using a continuous wave optical parametric oscillator (Argos Aculight) (OPO). The C-module provides a tunable source of infrared radiation in the CH stretch region with a narrow linewidth (less than 1 MHz) and an output power of over 3 W. The OPO idler frequency was stabilized to the $^1$R(1) branch transition at 3005.578 $cm^{-1}$ by locking to a Lamb-dip detected in a static gas absorption cell filled with 50 μbar of $CHD_3$ [16]. Almost 3 W of the OPO idler power was used for excitation of $CHD_3$ in the molecular beam from the initial state ($v$=0, $J$=1 and $K$=1) to the final state ($\nu_1$=1, $J$=2 and $K$=1) by RAP in order to maximize the excited fraction[13]. To achieve RAP, the OPO idler beam is focused by a cylindrical lens to create curved wavefronts of the IR field in the crossing region with the molecular beam. This wavefront curvature produces a frequency sweep due to the Doppler effect when the molecules in the molecular beam cross the excitation laser beam. With optimized conditions, this frequency sweep can be used to completely transfer the population from an initial rovibrational state to a final rovibrational state[13] by RAP. With the high velocity of the molecules in the present study ($v_{CHD_3}$ > 2400 $ms^{-1}$) and the Einstein coefficient for $\nu_1$ in $CHD_3$ (which is lower than for $\nu_3$ in $CH_4$ [17]), between 60% and 90% of the initial

rovibrational state population in the $CHD_3$ was transferred to the final rovibrational state through RAP, with the percentage decreasing with increasing molecular beam velocity.

### 1.4.1 Determination of $f_{exc}$

To determine the fraction of the incident $CHD_3$ prepared in the $\nu_1$=1, $J$=2 and $K$=1 rovibrational state, a room temperature pyroelectric detector was used. As this detector is only sensitive to changes in energy, the excitation laser was chopped at 2 Hz and a lock-in amplifier (Stanford Research Systems SR510) used to demodulate the signal. To be able to equate this signal to the flux of excited molecules, a calibration was done using a 3% $CH_4$ in He gas mix. We used $CH_4$ as fewer rotational levels have to be probed to determine the fraction of molecules in each rotational state.

For the calibration, we measured the total flux of $CH_4$ molecules into the UHV chamber with the same off-axis QMS (Pfeiffer QMG 422) that was used for the K&W measurements. $f_{\mathrm{exc}}$ was calculated as:

$$f_{\mathrm{exc}} = f_{\mathrm{rot}} f_{\mathrm{vib}} f_{\mathrm{RAP}} \qquad \text{(S1)}$$

where $f_{\mathrm{rot}}$ is the fraction of molecules in the initial rotational level, $f_{\mathrm{vib}}$ is the fraction of molecules in $v$=0 and $f_{\mathrm{RAP}}$ is the fraction of molecules in the ground rovibrational level excited through RAP. $f_{\mathrm{rot}}$ was determined by recording the fluence dependence of the pyroelectric detector signal for excitation of the $\nu_3$ antisymmetric stretch vibration for the four lowest rotational levels of ortho-$CH_4$ ($I_n$=1) *via* the R(1), R(2)-$F_2$, R(3)-$F_1$ and R(3)-$F_2$ transitions at $T_n$ = 298 K, 350 K and 400 K. The R(4)-$F_2$ transition was also probed, but no significant population was found in this state at the $T_n$ investigated. The fraction of molecules in the given rotational level was calculated as the ratio of the asymptotic pyroelectric detector signal for this level divided by the sum of the asymptotic

signals for all four levels at a given $T_n$. As the different nuclear spin isomers of $CH_4$ do not interconvert in a supersonic expansion[18], 9/16=56% of the molecules are in the ortho-$CH_4$ nuclear spin isomer. $f_{\mathrm{rot}}$ is given as the product of these two values.

$f_{\mathrm{vib}}$ was calculated from a Boltzmann distribution for a given $T_n$ neglecting vibrational cooling in the supersonic expansion. Since RAP was verified to cause complete population transfer from the initial rovibrational state to the final rovibrational state for the 3% $CH_4$ in He mix we used, $f_{\mathrm{RAP}}$=1. $f_{\mathrm{exc}}$ could then be determined using Eq. (S1), and the flux of excited molecules as the product of $f_{\mathrm{exc}}$ and total $CH_4$ flux. The pyroelectric detector signal was plotted against the flux of excited $CH_4$ molecules, which produced a linear calibration, as shown in Fig. S5. From this calibration performed for $CH_4$, the flux of vibrationally excited $CHD_3$ could be determined from the measurements of the pyroelectric detector signal presented here, taking into account the rovibrational energies of the $CHD_3$ ($\nu_1$=1) and $CH_4$ ($\nu_3$=1) states excited in the experiments. $f_{\mathrm{exc}}$ immediately follows as this flux value divided by the total flux of $CHD_3$ molecules into the UHV chamber.

### 1.5 The measurement of $S_0^{off}$, $S_0^{on}$ and the determination of $S_0^{\nu_1=1}$

The sticking coefficients were measured using the K&W beam reflectivity method[3,12]. This technique monitors the drop in partial pressure of $CHD_3$ by a QMS when an inert flag is removed from the molecular beam and molecules collide with the reactive surface, providing an accurate and self-calibrating way of obtaining $S_0$. In the measurements presented here, we monitored the change in partial pressure of mass 19. Experiments were also done monitoring mass 17 and the same value of $S_0$ was obtained, demonstrating that there was no other significant source of mass

19 which perturbed the measurements. We also confirmed that the response of the QMS to changes in partial pressure was linear over the range used in the experiments.

### 1.5.1 The King and Wells beam reflectivity method

A typical K&W trace is presented in Fig. S6, for a 1.5% $CHD_3$ in $H_2$ mix on Pt(111) with an incident translational energy of 82 kJ/mol, obtained for $T_n$=400 K, without laser excitation. A schematic of the molecular beam path is also shown in Fig. S7. The initial rise in the 19 amu signal at $t$ =-60 s corresponds to opening of the separation valve between the molecular beam source chamber and UHV chamber and the molecular beam being scattered from the inert flag. For $t$<0 s, the molecular beam is scattered by an inert beam flag which blocks the molecular beam from hitting the surface. The QMS signal obtained with the flag closed corresponds to a measurement of the total flux of the molecular beam. At $t$=0 s, the K&W flag is opened and the molecular beam hits the clean Pt surface, with the drop in the QMS signal due to the molecules that dissociate on the surface. At $t$=20 s the beam flag was closed again, and the separation valve shut at $t$=80 s. The sticking coefficient ($S(t)$) at time $t$ is given by:

$$S(t) = \frac{\Delta P(t)}{P} \qquad \text{(S2)}$$

where $P$ is the average partial pressure rise for $t$<0 s when the molecular beam scatters off the inert K&W flag, and $\Delta P(t)$ is the decrease in partial pressure at time $t$ after the beam flag is opened and the surface is exposed to the molecular beam for a time $t$. These changes in partial pressure are shown by arrows in Fig. S6.

$S_0^{on}$ was determined by the same methods as for $S_0^{off}$, except that a fraction of the incident $CHD_3$ was prepared state selectively in $\nu_1$=1, $J$=2 and $K$=1. Each sticking coefficient presented here is from the average of between two and five measurements.

### 1.5.2 Obtaining $S_0^{off}$, $S_0^{on}$ and $S_0^{\nu_1=1}$

To determine the average laser-on and laser-off sticking coefficients, $S_0^{on}$ and $S_0^{off}$, the time dependence of the QMS signal was fit using a double exponential decay[3]:

$$S(t) = A_1 e^{-k_1 t} + A_2 e^{-k_2 t} \quad \text{(S3)}$$

where $A_1 + A_2 = S_0$ and $k_i$ account for the rate at which the sticking coefficient decreases. The fits to the laser-off (black) and laser-on (red) data obtained using Eq. (S3) for the dissociation of $CHD_3$ on Pt(111) at an incident energy of 82 kJ/mol are shown in Fig. 1D as solid red and black lines respectively.

The value of $S_0^{on}$ in these measurements does not correspond to the quantum state resolved sticking coefficient for $\nu_1$, $S_0^{\nu_1=1}$. This is because not all the $CHD_3$ in the incident molecular beam is vibrationally excited, and the molecules that are not excited by the laser can still make a significant contribution to the observed reactivity. $S_0^{\nu_1=1}$ is calculated from [19,20]:

$$S_0^{\nu_1=1} = \frac{S_0^{on} - S_0^{off}}{f_{\text{exc}}} + S_0^{v=0} \quad \text{(S4)}$$

where $S_0^{v=0}$ is the sticking coefficient for molecules in the vibrational ground state, $v$=0.

### 1.5.3 Obtaining $S_0^{v=0}$

To determine the state resolved sticking coefficient, $S_0^{\nu_1=1}$ using Eq. (S4), $S_0^{v=0}$ is needed. At the highest nozzle temperature used for the laser-on measurements ($T_n$=500 K) and assuming a Boltzmann distribution at $T_n$ for the vibrational level populations, we estimate that 80% of $CHD_3$ molecules are in the vibrational ground state $v$=0 and the remainder in low lying bending vibrations. We therefore assume that the measured average laser-off sticking coefficient is a close upper limit to $S_0^{v=0}$ and use $S_0^{off}$ instead of $S_0^{v=0}$ when calculating $S_0^{\nu_1=1}$[11]. To investigate the

validity of this, both $S_0^{off}$ and $S_0^{v=0}$ were computed from the AIMD calculations, and the difference between the values found to be within the error bars of the experiment.

## 1.6 Influence of adsorbates on the measurements of $S_0$

The surface reactivity of $CHD_3$ was measured on Pt(111) at $T_s$=500 K and for Pt(211) at $T_s$=650 K. These surface temperatures were used as they are sufficiently above 400 K where hydrogen recombinatively desorbs from Pt(111) and Pt(211)[21–24] preventing passivation of the surface by adsorbed H. Different temperatures were used for the two surfaces as CO molecularly desorbs from Pt(111) at $T_s$=450 K[25,26] and from Pt(211) at $T_s$=600 K[27,28]. We chose to work at 50 K above these desorption temperatures so any trace contaminant of CO in the molecular beam will not passivate the surface.

On the Pt(111) surface, recombinative desorption of $CH_3$(ads) with H(ads) atoms to produce $CH_4$(g) has been observed at surface temperatures above 240 K[22], which could potentially lead to a loss of $CH_3$(ads) and lead to an underestimation of the sticking coefficients. As the methyl fragments will dehydrogenate more quickly at $T_s$= 500 K[29] than at $T_s$=240 K, and H(ads) desorbs by recombinative desorption as $H_2$(g)[21,22], the recombinative desorption of the dissociated methane will not occur significantly in the measurements presented here. For Pt(211), TPD measurements showed that $CH_3$(ads) dehydrogenates below 550 K, leading to the conclusion that recombination is also negligible for the Pt(211) surface.

## 1.7 Additional experimental considerations

The measurement of $S_0$ at high incident kinetic energies presents a number of experimental challenges, the first of which is to create a fast molecular beam. High $E_i$ can be achieved by using

a light carrier gas, by increasing the nozzle temperature, or a combination thereof. Raising $T_n$ increases the population of the low lying vibrationally excited states, which is problematic for the AIMD calculations (see Sec. 2.1). Therefore, we use a dilute mixture of $CHD_3$ in $H_2$ instead of He, as the same incident energy can be achieved at a lower nozzle temperature. Seeding in $H_2$ however restricts the measurements to $T_s$ > 400 K in order to prevent the surface passivation by adsorbed H atoms[21–24].

Another advantage of seeding in $H_2$ is the lower $T_n$ needed leads to a higher population of $v$=0 which results in a larger $f_{\mathrm{exc}}$ for the laser-on measurements. As can be seen from Eq. (S4), the difference between $S_0^{off}$ and $S_0^{on}$ is dependent on $S_0^{\nu_1=1} \times f_{\mathrm{exc}}$, so a larger $f_{\mathrm{exc}}$ gives a larger difference between the laser-on and laser-off measurements. With increasing nozzle temperatures, $f_{\mathrm{exc}}$ decreases as there are fewer molecules in the initial rovibrational state to excite, and as RAP becomes less efficient for faster molecular beams. $S_0^{off}$ also gets larger with increasing nozzle temperature as the population of the low lying vibrational levels increases. These two factors combined make the measurement of $S_0^{\nu_1=1}$ at high $T_n$ experimentally challenging, leading to a preference for $H_2$ over He as seed gas since it allows us to reach a given $E_i$ at lower $T_n$.

The final limiting factor in the determination of the state resolved sticking coefficients is how strongly vibrational excitation promotes the reactivity of the molecules. On Ni(111), the $\nu_3$ vibrational efficacy (η) for the dissociation of $CH_4$ is high (η=1.25[30]), i.e. vibrational energy promotes the reactivity more strongly than translational energy. On Pt(111), the efficacy is less than one (η=0.7[3,8]) i.e. vibrational excitation promotes the reactivity less efficiently than translation. This reduces the translational energy range over which it is possible to accurately measure state resolved sticking coefficients. For the Pt(211) measurements $S_0^{\nu_1=1}$ does not change significantly over the range of translational energies it was measured, suggesting that the value

obtained is close to its asymptotic value. As $S_0^{off}$ was still increasing exponentially, the difference between $S_0^{off}$ and $S_0^{on}$ decreased with increasing $E_i$ more rapidly than in the Pt(111) measurements, reducing the range of energies over which we could determine state resolved sticking coefficients on Pt(211).

## 2. Theoretical methods.

Here we describe the SRP-DFT methodology used for $CHD_3$ on Pt. The implementation used for $CHD_3$ on Ni(111) has been discussed in detail in Ref.[11].

### 2.1 Joint experimental-theoretical strategy

In this work we exploit the semi-empirical DFT approach called SRP-DFT[31] that has been proven successful on different molecule-metal surface systems such as $H_2$ on Cu(111)[32], $H_2$ on Cu(100)[33], $D_2$ on Pt(111)[34] and recently $CHD_3$ on Ni(111)[11]. The standard procedure to develop an SRP functional is to mix two standard GGA density functionals by tuning a single parameter in order to fit the outcome of simulations to a particular experimental observable that depends on the minimum barrier height (e.g., $S_0^{off}$) and then to validate the functional by reproducing different experiments (e.g., $S_0^{v_1=1}$) on the same system. More recently the SRP approach has used a GGA exchange functional but a non-local correlation functional[35,36]. The main aspects of the approach are discussed here and in the following sections while more details can be found in Ref[11].

AIMD[5,37] is used to develop and test the SRP functional exploiting the quasi-classical trajectory (QCT) approach, in which vibrational zero-point energy (ZPE) is initially imparted to the molecule. For the experimental conditions we address, AIMD-QCT is the method of choice to effectively simulate molecular beam experiments and to test the validity of the semi-empirical SRP

approach we are developing. The main reason to choose AIMD over a higher level of theory (i.e., quantum dynamics)[38–44] is the possibility to include explicitly in the simulation all the degrees of freedom (DOF) of the system without any dynamical approximations. Not only is it possible to include all the molecular DOFs, but the surface atom motion, which is known to be important for the dissociation of methane on metal surfaces[45], is also accounted for. Another advantage of AIMD is that the forces are computed on-the-fly on a DFT level without the need to fit a high dimensional potential energy surface (PES). Extension to reactions affected by electron-hole pair excitation, which is not expected to be important for the systems treated here[46], are possible by combining SRP-DFT with AIMD methods that include electronic friction[47]. Due to limits to present-day computational resources, AIMD cannot be comfortably used to compute reaction probabilities < 1%. However, as recently demonstrated for $N_2$ + Ru(0001) high dimensional PESs also describing the motion of the surface atoms can now be obtained with a neural network approach[48], which also can be coupled with the SRP scheme.

In order to ensure a meaningful comparison between experiments and AIMD-QCT simulations, many aspects have to be considered, both on the experimental and on the theoretical side. First, the total energy of the molecule (translational + vibrational) has been chosen to be well above the minimum ZPE corrected barrier. This ensures the applicability of the QCT approach because under such conditions the reaction occurs in the classical "over-the-barrier" regime[5,49]. Second, the molecular beams have been produced using $T_n$ as low as possible, taking advantage of $H_2$ seeding, so that most of the molecules (from 60% to 97%, depending on $T_n$) are in the vibrational ground state. This limits the deficiencies of the QCT method in describing the reactivity of CD excited vibrational states due to artificial intramolecular vibrational energy redistribution (IVR) caused by the availability of resonant vibrations[11]. For the same reason the $\nu_1$=1 excited

state of $CHD_3$ has been chosen to compare theoretical and experimental state selected reaction probabilities. This excited vibrational state possesses 95% of CH stretch character[50] and, due to the lack of Fermi resonances, energy imparted to this normal mode in the gas phase remains localized on a time scale comparable with the collision time[11,51]. The reactivity of $\nu_1$=1 $CHD_3$ is therefore unlikely to be affected by IVR[5,51]. Third, the $T_s$ has been chosen well above the Debye temperature ($T_D$) of platinum bulk (i.e. 234 K)[52] and therefore also above $T_D$ for the Pt(111) (estimated to be between 111 and 143 K)[53–55] and the Pt(211) surfaces. At $T_s$>$T_D$ quantum effects are not expected to significantly affect the molecule-surface energy exchange dynamics, making such conditions suitable for AIMD simulations.

Specifically, for values of $T_s$ higher than the Debye-Waller temperature the validity of a classical approach to dynamics calculations on scattering from a surface can be assessed by computing the argument to the Debye-Waller factor[56] $\left(2W = \frac{3p^2 T_S}{M_C k_b T_D^2}\right)$, where $p^2$ is the average of the square of the change in momentum of a scattering molecule, $M_C$ the mass of a surface atom and $k_b$ the Boltzmann constant. Experience suggests that treating the surface vibrations classically works well for $T_s > T_D$ for values of $2W$ greater than 6[57,58] (note that 2W is a dimensionless quantity). For methane scattering from Pt(111) and Pt(211) at the lowest $\langle E_i \rangle$ investigated under laser-off conditions (81.7 kJ/mol and 58.2 kJ/mol for Pt(111) and Pt(211), respectively), our calculations show a values of about 240 and 150 (for Pt(111) and Pt(211), respectively) for the Debye Waller argument $2W$. This suggests that, under the conditions we are investigating, the energy transfer to the surface phonons happens classically.

In addition, the experiments have been performed using well defined beam parameters and $T_n$ (see Table S2) allowing an accurate sampling of the initial collision energy and of the rovibrational population in the simulations.

## 2.2 SRP density functional approach

The semi-empirical method we are using is a variant of the SRP approach originally proposed by Truhlar and coworkers[31,59]. Our SRP implementation allows improvement over the accuracy of standard GGA functionals, which is in general not quantitative for molecule-surface systems. The SRP strategy consists of selecting an experimental observable that depends on the minimum barrier height, in our case $S_0$, and to choose two functionals that predict $S_0$ values that are systematically too high and too low compared to the experimental data. For many molecules reacting on a metal surface[32,40,60–64] the exchange functionals of choice are PBE[65] and RPBE[66], with the first known to usually underestimate and the second to overestimate barrier heights for these systems when combined with the PBE correlation functional (Eq. (S5), below) or a non-local vdW correlation functional (Eq. (S6), below). The SRP exchange correlation functional ($E_{XC}^{SRP}$) is then defined as a linear combination of the chosen GGA functionals:

$$E_{XC}^{SRP} = x \cdot E_{XC}^{RPBE} + (1 - x) \cdot E_{XC}^{PBE} \qquad \text{(S5)}$$

where *x* is an adjustable parameter that allows us to tune the performance of the functional in order to fit theoretical $S_0$ values to a set of experimental results. Once the mixing parameter is identified the SRP functional is tested and validated by simulating a different set of experimental data (in our case initial-state selected reaction of $CHD_3$ in $\nu_1$=1).

As already successfully applied to $CHD_3$ on Ni(111)[11], the van der Waals interaction can be accounted for by replacing the PBE correlation functional present in PBE and RPBE by the vdW-DF correlation functional ($E_C^{\text{vdW-DF}}$) developed by Dion et al.[35,67]. This correlation functional has been shown to improve the description of weakly activated dissociation[63] while maintaining the same accuracy of[68], or improving the accuracy[11] over that achieved using Eq. (S5) for highly activated dissociation systems. In addition, the vdW-DF correlation functional is non-empirical

being based on first principles[69]. The general formulation of the SRP functional used in this and previous work[11] uses a linear combination of the two GGA exchange functionals ($E_X$) plus vdW-DF correlation:

$$E_{XC}^{SRP} = [x \cdot E_X^{RPBE} + (1-x) \cdot E_X^{PBE}] + E_C^{\text{vdW-DF}} \quad \text{(S6)}$$

The SRP functional is constructed as much as possible[11] on the basis of non-empirical, constrained-based functionals (including the spin-scaling relationship, the Lieb-Oxford bound, and the recovery of the uniform gas limit[35,65] that should ensure applicability to metals [70]).

2.3 Influence of the spin-polarized implementation of the vdW correlation functional on the barrier energy for $CH_4$ + Ni(111)

The nonlocal correlation functional that has been proposed by Dion *et al.*[35] to account for van der Waals interactions has originally been formulated in a spin-restricted formalism. A first implementation that has appeared in electronic structure codes and that allowed for spin-polarized vdW-DF calculations consisted in evaluating the (spin-unpolarized) nonlocal correlation functional from Ref.[35] based on the total electron density (spin up density + spin down density). In previous work[11], we have used this spin-polarized generalization of the otherwise spin-unpolarized vdW correlation functional as implemented in VASP 5.3.5 in order to fit the SRP functional to experimental dissociation probabilities for $CHD_3$ on Ni(111) (SRP32-vdW, i.e. Eq. (S6) with $x$=0.32). We show here that the SRP32-vdW minimum energy barrier for methane dissociation on Ni(111) does not significantly change if the recently proposed extension of the vdW nonlocal correlation to spin-polarized systems by Thonhauser et al.[71] is employed instead. These findings suggest that the SRP32-vdW functional should accurately describe the reaction of

methane on Ni(111) also if paired to the more rigorously derived spin-polarized implementation of the vdW correlation functional from Ref.[71].

We have used here the minimum energy barrier geometry as obtained earlier through climbing image nudged elastic band (CI-NEB) calculations for $CH_4$ reacting on Ni(111)[11]. In order to perform DFT calculations using the spin-polarized extension of the vdW correlation functional from Ref.[71], we have employed the quantum ESPRESSO (QE) DFT package[72], where we have implemented the exchange part of the SRP32-vdW functional through a modified version of the LIBXC exchange-correlation functional library[73]. Projector augmented wave (PAW)[74,75] potentials from the pseudopotential library pslibrary[76] (version 1.0.0) have been employed, with an energy cut off for the plane wave expansion corresponding to 46 Ry (1 Ry ≈ 13.606 eV ≈ 1312.75 kJ/mol). All the other computational parameters (k-points, smearing, number of atomic layers, etc.) have been set as in the VASP calculations performed in Ref.[11]. A vacuum space of 13 Å has been employed to separate periodic replicas of the slab. The barrier energies ($E_b$ values) reported in Table S3 are calculated as the difference between the total energy of the transition state configuration and the total energy of the asymptotic configuration, in which a molecule in its equilibrium geometry is placed 6 Å away from the surface. Considering that the purpose here is to compare functionals (and functional implementations) for given geometries, we find it instructive to also include in the comparison presented below $E_b$ values calculated with the PBE functional[65,77] and with the original formulation[35] of the vdW-DF[69,71,78,79] functional (i.e. with revPBE exchange[80]) while using the SRP32-vdW transition state geometry and lattice constant.

The results are summarized in Table S3 (note that the reported barrier heights are not yet corrected for the finite interaction the molecule still has with the surface at Z = 6 Å, in contrast to the values reported in the main paper, but this does not affect the comparison for the present

purpose). VASP and QE predict very similar $E_b$ values for all the functionals investigated. When using the PBE functional, the two codes return energies for the considered transition state geometry that differ by only 0.2 kJ/mol. We take this to imply that the pseudopotentials used in the VASP and QE calculations are of a very similar quality, and that the use of the different pseudopotentials by itself should not lead to different energetics beyond a few tenths of a kJ/mol. For the two functionals that make use of the vdW correlation, i.e. the vdW-DF and the SRP32-vdW functionals, the agreement is still very good (the difference is about 1 kJ/mol, i.e. less than 0.25 kcal/mol), which suggests that the two vdW correlation implementations for spin-polarized systems do not predict significantly different energetics for methane reacting on Ni(111). In view of this small energy difference, we argue that using the earlier VASP implementation of the vdW correlation functional (and not yet the spin-polarized adapted version of Ref.[71]), and subsequently using the SRP density functional derived in this way also for $CHD_3$ + Pt(111), was justified, and should not lead to changes of any of our main conclusions.

## 2.4 Electronic structure calculations

All the DFT calculations (excluding the QE calculations reported in Sec. 2.3) have been performed using the VASP code (version 5.3.5)[81,82]. The plane wave basis set expansion has been cut off at 350 eV and a 0.1 eV wide Fermi smearing has been used to facilitate the convergence. The core electrons have been described through the PAW[74,75] method; the pseudopotentials used have been generated with the PBE functional and model explicitly 4 and 10 valence electrons for C and Pt, respectively. The first Brillouin zone has been sampled with a 4x4x1 Γ-centered k-point grid. This setup has been tested for accuracy as described in the following paragraphs.

The Pt bulk lattice constant has been optimized with the SRP32-vdW functional and the result (i.e., 4.02 Å) is in reasonable agreement (difference of 2.7 %) with the experimental value of 3.92 Å[83,84].

The transition state (TS) geometries have been determined using the dimer method as implemented in the VASP transition state tools (VTST) package[85–88] by Henkelman and Jónsson. The search for the TS has been started from the TS geometries on Pt(111) previously found by Jackson and coworkers[89,90] and all 15 molecular DOFs have been optimized while keeping the surface frozen in its relaxed 0 K configuration. The optimization of the TS geometries has been stopped when the maximum force on any degree of freedom was smaller than 5 meV/Å. All the TS geometries reported and discussed in this work (except where stated differently) have been proven to be first order saddle points in the molecular coordinate space through frequency analysis (by checking that one and only one imaginary frequency was found).

The barrier height has been computed as $E_b = \varepsilon_{TS} - \varepsilon_{asym}$; here, $\varepsilon_{TS}$ is the absolute energy of the transition state geometry and $\varepsilon_{asym}$ is the absolute energy of the system with the molecule in the gas phase. The gas phase geometry consists of the optimized molecule placed in the vacuum far from the slab: 6 Å above the surface for Pt(111) and 6.5 Å above the step edge atoms for Pt(211).

## 2.5 Pt(111) surface and convergence tests

The supercell used in the calculations on Pt(111) is very similar to the one used in previous work[11,64] namely a (3x3) unit cell with 13 Å of vacuum separating the slab from its first periodic image, here we used 5 layers instead of the 4 used to model the Ni(111) slab[11]. The convergence of the computational setup has been tested with respect to the number of layers, the cell size, the

cut off energy and the k-point sampling by comparing computed minimum energy barrier heights. The results, reported in Table S4, show that the setup we use predicts converged barrier heights, which change by only 5 meV if a converged setup with 6 layers, a 4x4 unit cell, a 350 eV cut off and 4x4x1 k-points is employed. The size of the vacuum used in the simulations is extensively discussed below in Sec. 3.

### 2.6 Pt(211) surface and convergence tests

The primitive unit cell of the Pt(211) slab contains 3 atoms per layer that we name edge (on the step edge), middle (in the center of the (111)-like terrace) and bottom (on the lower side of the step edge) atoms (see Figs. 1B and 1C). These atoms describe the width of the (111)-like terrace along the x direction, while the step runs along the y direction (see Fig. S8). The primitive cell is rectangular and the cell vector in the x direction is roughly 2.4 times larger than the one in the y direction. In this work a 4 layers (1x3) cell has been used (top view depicted in Fig. S8 and Fig. 1C). The slab geometry has been optimized in all the degrees of freedom and a small contraction of the surface has been observed. The angle between the normal to the (111) terrace and the z axis is $\varphi$=16° which compares with $\varphi$=19.5° for the unrelaxed geometry[91].

Convergence tests have been performed on the minimum barrier height for plane-wave cut off, k-points sampling, number of layers and the size of the cell. The test has been performed on the TS geometry for a molecule dissociating above the step edge atom with the reacting bond oriented along the step edge direction (y) (see Fig. S8). The results, summarized in Table S5, show that the barrier computed with the selected cell size matches the one obtained with a converged and much larger cell (i.e. 2x4, 5 layers). The k-point grid and cut off energy used for the Pt(111) surface are also reasonably accurate for the Pt(211) surface. The chosen setup (1x3 cell, 4 layers,

350 eV cut off, 4x4x1 k-points) returns the same energy barrier within 7 meV of the largest and best converged setup (2x4 cell, 5 layers, 500 eV cut off, 8x8x1 k-points).

## 2.7 Quality of the QCT method for comparison with present experiments

In Sec. 2.6 of the Supporting Information (SI) to Ref.[11], an extensive argument was provided for why the QCT method for treating the $CHD_3$ dynamics should be quite suitable for accurately describing the experiments presented here. For the details of the argument we refer to Ref.[11], here we only provide a summary. First, calculations on $D_2$ + Cu(111) have shown that, if all molecular degrees of freedom are included in the dynamics calculations, QCT calculations essentially reproduce quantum dynamical reaction probabilities for translational energies above the zero-point energy corrected minimum barrier height ( see Ref.[92], for instance the left panels of Fig. 5 therein). Because the frequencies and the reduced masses of the $\nu_1$=1 CH-stretch vibration of $CHD_3$ and the vibration of $D_2$ are very similar, it is quite likely that the same is true for $CHD_3$. Second, the reaction of $CHD_3$ ($\nu_1$=1) is unlikely to be affected by artificial energy transfer from the initially excited CH-stretch vibration to the other vibrational modes in the isolated molecule, because the CH-stretch frequency is isolated from that of the other vibrations. Third, as summarized in Ref.[11] all available evidence suggests that for the conditions we address the QCT approach is not invalidated by problems related to quantum effects, such as zero-point energy violation, or the neglect of tunneling. Fourth, comparisons of quantum dynamical (QD) calculations to high dimensional QCT calculations that suggested discrepancies between QD and QCT results have often been based on either different dynamical models (for instance, involving different numbers of degrees of freedom) or different potential energy surfaces, thereby raising doubts on the conclusion arrived at regarding the reliability of QCT. In summary (again, for details

and references consult Sec. 2.6 of the SI to Ref.[11]), all solid evidence presently available suggests that the QCT approach to the $CHD_3$ dynamics in the AIMD calculations should be accurate and reliable for the reactions studied and the experimental conditions addressed in this work.

## 3. Construction of the SRP density functional

### 3.1 Asymptotic residual energy correction

In our AIMD calculations using the vdW correlation functional, the asymptotic energy of $CHD_3$ far from the surface is not completely converged since the long-range interaction modelled by the vdW-DF correlation would require a vacuum space between the slab periodic images much larger than the 13 Å used, which would make the AIMD calculations very expensive. This limitation can however be overcome, as already implemented earlier for $CHD_3$ on Ni(111)[11]. To a very good approximation, using a smaller amount of vacuum (13 Å instead of a well-converged value of 30 Å) affects the energy of the system only as a small upwards shift of the gas phase level, due to residual interaction with the slab and its periodic replica, as sketched in Fig. S9. On the Pt(111) surface the residual interaction ($E_R$) is defined as the difference between the energy of the molecule placed 6 Å away from the surface, i.e. where it sits at the beginning of the simulations, in the cell with 13 Å and 30 Å of vacuum:

$$E_R = E_{Z=6\text{Å}}^{13\text{Å}} - E_{Z=6\text{Å}}^{30\text{Å}} \approx \Delta E_b = E_b^{13\text{Å}} - E_b^{30\text{Å}} \qquad \text{(S7)}$$

$E_R$ has been checked to be the same, to within much better than chemical accuracy (i.e., about 1 kJ/mol), as the difference in the minimum barrier height ($\Delta E_b$) computed with the two cell sizes ($E_b^{13\text{Å}}$ and $E_b^{30\text{Å}}$, respectively). Note that to compute the barrier height for the set up using 30 Å of vacuum length, the molecule is put at Z = 15 Å in the asymptotic geometry.

In order to correct for the residual interaction in the AIMD simulations, in the present work and in the previous work on Ni(111)[11] the molecules are assigned an extra translational energy equal to $E_R$ which, for the system investigated, is on the order of a few of kJ/mol. By imparting this excess energy, the molecules experience an effective barrier ($E_b^e$) that is approximately equal to the converged barrier height $E_b^{30\text{Å}}$ :

$$E_b^e = E_b^{13\text{Å}} - E_R \approx E_b^{30\text{Å}} \quad \text{(S8)}$$

3.2 van der Waals interaction and effective barriers

For $CHD_3$ on Pt(111) the residual interaction $E_R$ (see Eq. (S8)) has been calculated with the SRP32-vdW functional. The interaction of methane in its gas-phase geometry ($\beta$ = 180°, one hydrogen pointing towards the surface) with the surface has been calculated as a function of the distance (Z) comparing the results obtained with 13 Å and 30 Å of vacuum. The computed residual interaction energy $E_R$ (see also Fig. S10) is equal to 4.0 kJ/mol. This result is similar to that found earlier for $CHD_3$ on Ni(111) with the same SRP32-vdW functional ($E_R$=3.9 kJ/mol) [11]. In the AIMD simulations, 4.0 kJ/mol is therefore the extra translational energy that has been assigned to the molecules in the Pt(111) dynamics to account for the not-converged vacuum size. In order to check the quality of the correction applied we compare the barriers using 30 Å of vacuum and an asymptotic molecule-surface distance of 15 Å ($E_b^{30\text{Å}}$) and the effective barrier ($E_b^e$) calculated according to Eq. (S8). For the SRP32-vdW the difference is about 1 kJ/mol validating our approach. The results are reported in Table S6. Note that the best estimate of the semi-empirical barrier height obtained from the comparison of our AIMD calculations to experiments corresponds to $E_b^e$, but that fully converged calculations with the SRP32-vdW functional (i.e., using a large

enough vacuum distance and asymptotic molecule-surface distance) would be expected to result in a barrier height closer to $E_b^{30\text{Å}}$.

For $CHD_3$ on Pt(211) the long range interaction has also been investigated and the results are reported in Fig. S11. For this stepped surface, Z is defined as the distance from the center of mass of the molecule to the (211) surface plane (taken as the z coordinate of the step edge atoms). With this definition, the distance from the (211) surface of course does not depend on the x coordinate of the molecule, but the distance to the closest Pt atom does depend on where the molecule is placed. The long-range interaction has been studied for the three non-equivalent top sites, i.e, edge, middle and bottom (see Fig. S8). At a large distance from the surface, the molecule-surface interaction is expected to be almost independent of the lateral displacement of the molecule, and in fact, we find for the three impact sites asymptotic energies that differ by just 0.1 kJ/mol. Comparing the results obtained with the 13 Å to the 30 Å vacuum set up, we found that the residual energy at 6.5 Å for the (211) surface is $E_R$=2±0.2 kJ/mol depending on the impact site. Once again, the quality of the residual energy correction is confirmed by the fact that the effective barrier $E_b^e$=52.6 kJ/mol differs by just 1.2 kJ/mol from the converged $E_b^{30\text{Å}}$ (=51.4 kJ/mol). The results for both Pt(111) and Pt(211) are summarized in Table S6.

### 3.3 van der Waals adsorption well

To search for the most stable molecular adsorption site on the Pt(111) surface we optimized 40 randomly oriented $CH_4$ molecules above the hollow site and 40 above the top site in these calculations and in the calculations on Pt(211) reported in this section, we have used the DFT setup with the vacuum of 13 Å. However, we have added the asymptotic correction $E_R$ to obtain reliable values of the well depth (see Sec. 3.2). Above the hollow site all the optimized geometries cluster

in three groups according to the adsorption energy. These clusters also differ by the number of H atoms pointing towards the surface. The more H atoms are pointing towards the surface the deeper is the well.

For each cluster the most stable geometry shows an adsorption energy ($E_{ads}$) of 21.9, 20.3 and 18.3 kJ/mol for three, two and one hydrogens pointing towards the surface, respectively. In the most stable geometry the molecule sits above a hollow site with three H atoms pointing towards the three top sites (eclipsed configuration). The potential is rather flat in the proximity of these minima; in fact within each cluster we find optimized geometries with slightly different orientations but with the same, or very similar, energy.

The maximum ΔE within one cluster is observed when the most stable geometry is rotated by 60° so that the H atoms point towards bridge sites (staggered configuration). The staggered configurations show an adsorption energy that is only 0.3 kJ/mol lower than the eclipsed configuration.

The same considerations apply to the top site and the same clustering is observed; however, the adsorption energies are generally lower. The deepest well for each cluster shows $E_{ads}$ = 21.2, 20.3, 19.4 kJ/mol for three, two and one H atoms pointing towards the surface, respectively. The largest value of the well depth is reported in Table S7 and shows good agreement with the experimental value of 18 kJ/mol[93].

The same search has been carried out focusing on the three non-equivalent top sites (bottom, middle and edge) of the Pt(211) surface by optimizing 40 randomly oriented $CH_4$ molecules on each site. On the bottom chain we find the two most stable adsorption geometries with the same $E_{ads}$ = 24.8 kJ/mol, one on a top site and the other on a hollow site. In both cases the molecule has three H atoms pointing towards the surface. On the edge chain the potential has been

found to be particularly flat as many adsorption geometries with different orientations have been found with very similar adsorption energies. The largest $E_{ads}$ found on the edge chain is 18.2 kJ/mol but all the adsorption energies fall within 1.2 kJ/mol. No stable adsorption site was found on the middle chain. The most stable adsorption states for the three surfaces considered (i.e., Ni(111), Pt(111) and Pt(211)) are sketched in Fig. S12, and reported and compared with experiment in Table S7.

## 4. AIMD calculations

### 4.1 AIMD setup and initial condition sampling

We have performed AIMD calculations simulating a microcanonical (NVE) ensemble where a $CHD_3$ molecule is impinging on the metal slab equilibrated at the experimental surface temperature $T_s$. The molecules impinge perpendicularly to the Pt(111) and the Pt(211) surface plane and are propagated with a time-step of 0.4 fs until an outcome (reaction, scattering or trapping, as defined in Sec. 4.2) is reached.

Ten Pt(111) slabs have been initialized expanding the lattice constant by the thermal expansion coefficient (i.e., 1.004[83]) in a procedure used previously[11,60] and assigning random displacements and velocities to the atoms according to an independent harmonic oscillators model. The ten slabs have then been equilibrated through a 2 ps dynamics with a 1 fs time-step while monitoring the temperature. For each $CHD_3$ + Pt(111) trajectory the initial surface atom positions and velocities are randomly chosen from the configuration assumed in one of the last 1000 steps of the ten equilibration dynamics runs. The average temperature $\langle T_s \rangle$ that corresponds to this pool of configurations is 478.6 K with a standard deviation of $\sigma$=47.0 K. Ten equilibrated slabs have been prepared analogously for Pt(211) at $T_s$ = 650 K (using a thermal expansion coefficient of

1.005[83]) obtaining a pool of configurations with $\langle T_S \rangle$ = 642.7 K and σ=74.8 K. In order to check whether the step geometry is properly maintained and represented during the AIMD simulations the angle between the normal to the (111) terrace and the Z axis (φ) (equal to = 16° for the optimized 0 K slab) has been monitored through the equilibration runs obtaining $\langle \varphi \rangle$ = 15.61 ± 1.27°. In all the equilibration dynamics and the molecule-surface trajectories the lowermost layer is frozen while the atoms in the uppermost layers (4 and 3 for Pt(111) and Pt(211), respectively) are free to move in all their DOFs.

The molecular initial conditions have been set up following the same procedure previously used for $CHD_3$ on Ni(111) and summarized in this section. Further details can be found in Ref.[11]. In order to select the initial translational energy of the molecules the experimental beam energy distributions have been sampled (the experimental beam parameters, i.e. the stream velocity and broadening, are provided in Table S2). The residual energy $E_R$ (i.e. 4 and 2 kJ/mol for Pt(111) and Pt(211), respectively) has been added to the translational energy of the molecule in order to correct for the residual interaction (see Sec. 3). The QCT method has been implemented by imparting ZPE to the vibrational modes of the molecule. In order to simulate the laser-off beams the initial vibrational state of the molecule is sampled from a Boltzmann distribution at $T_n$ while its angular momentum has been initially set to zero, and the molecule's orientation has been randomly sampled.

In order to simulate $\nu_1$=1 beams all the molecules have been initialized with one quantum of energy in the CH stretch mode. Experimentally the molecules have been excited through the $^1$R(1) transition populating the rotational state $J$=2, $K$=1 which we have simulated in the AIMD trajectories. Since in the experimental setup the laser excitation happens relatively far from the surface (the flight time from the excitation to the surface is a few hundreds of μs) any alignment

in $M$ should be erased by hyperfine coupling[94] and therefore, in the simulations, $M$ has been statistically sampled among all the accessible states (i.e. $M$=-2, -1, 0, 1, 2) as done previously for $CHD_3$ on Ni(111)[11]. The initial center of mass position has been chosen randomly in XY to uniformly sample the whole unit cell and Z being 6.0 Å or 6.5 Å for Pt(111) and Pt(211), respectively.

## 4.2 AIMD sticking probability and outcome definition

To analyze the results three possible outcomes have been defined for the trajectories: scattering, reaction and trapping. The molecule has been considered scattered if the Z-coordinate of its center of mass is the same as in the initial gas phase geometry (6.0 and 6.5 Å for Pt(111) and Pt(211), respectively) and the velocity of the center of mass is pointing away from the surface. The molecule has been considered reacted when one of the bonds was longer than 3 Å. If none of the cited outcomes was reached within the first ps of propagation the molecule has been considered trapped.

The reaction probability ($p_i$) for the average beam energy $\langle E_i \rangle$ and the nozzle temperature $T_n$ has been computed as $p_i = N_r / N_i$ , where $N_r$ is the number of reacted trajectories and $N_i$ is the total number of trajectories for that particular $\langle E_i \rangle$ and $T_n$. The standard errors associated with the reaction probability $p_i$ has been computed as $\sigma = \sqrt{p_i(1 - p_i)/N_i}$. The total number of trajectories $N_i$ for each $\langle E_i \rangle$ has been chosen in order to have error bars comparable to the experimental data (see Table S8).

4.3 Statistical test based on Stouffer's Z-score

As in Ref.[11], a statistical test based on the Stouffer's Z-score[95] has been used to also put the comparison of the theory and the experiments on a statistical basis. Such tests are based on a hypothesis that assumes that theory reproduces experiments. Then, one expects that Stouffer's Z-score $\left(Z_{comp} = \sqrt{1/k}\sum_{i=1}^{k}\frac{P_i(AIMD)-P_i(\exp)}{\sigma_i}\right)$ shows a value close to zero. Here, k is the number of experiments involved in the test, $P_i(AIMD)$ the computed reaction probability for the i$^{th}$ experiment, $P_i(exp)$ the experimental value, and $\sigma_i$ is the standard error in the difference. The experimental error was evaluated from the differences between repeated measurements. In our test based on this statistic, first a required significance level (α) is set, which corresponds to a specific value of the probability that we discard our hypothesis even though it might be true. The hypothesis is rejected if the absolute value of the calculated test statistic differs from zero by more than the corresponding threshold value (i.e., if the corresponding probability, which we call the p-value, is less than α). Working with small α values is therefore equivalent to requiring considerable statistical evidence for the hypothesis to be rejected. We work here with α = 0.10, i.e., 10%, therefore we only reject our hypothesis with reasonably strong statistical evidence to the contrary. Stouffer's Z-score test is appropriate if theory and experiment shows similarly sized error bars. Note that this test cannot be formulated in the more often used way, where a null hypothesis is formulated that may be viewed as a counter-claim to what one hopes to prove, and one then proceeds to show that the counter-claim is unlikely to be valid. This is because a Z-score-based test like the Stouffer's method requires the test statistic to follow a normal distribution under the null hypothesis and this formulation is incompatible with our 'counter-claim' statement ("theory and experiment disagree") being the null hypothesis and the test statistic being a measure of the difference between theory and experiment: evidence for such a test statistic to follow a normal

distribution would instead indicate that “theory and experiment agree”, implying that it is not possible to use the opposite statement (the counter claim) as null hypothesis. More details are in the SI to Ref.[11].

Finally, we note that, of course, the statistical test by itself cannot "prove" that the AIMD and experimental results agree with one another. Rather, as used here it provides us with a probability that the observed statistical outcome is consistent with the hypothesis that "the AIMD and the experimental results agree with one another to within statistical error bars". In the present context, the statistical test is best used in a conservative way, i.e., to reject the hypothesis that the experiment and the theory are in agreement with one another if there is reasonably strong evidence to the contrary. The ultimate verdict on the accuracy with which experiment reproduces theory should therefore not only be based on this test and the computed p-value, but also on the agreement between theory and experiment as observed visually, and the average distance along the energy axes between the computed reaction probability and the fitted experimental reaction probability curve (chemical accuracy is achieved if this is less than 1 kcal/mol).

## 5. AIMD results

### 5.1 Comparison of AIMD and experimental sticking coefficients

The experimental $S_0$ values reported in Table S8 are reported in Fig. S13 together with all the available experimental data on $CHD_3$ + Pt(111). The differences noted between the laser-off experiments of 2013[5] and the present experiments (2016) at similar $E_i$ are probably mostly due to the use of different $T_n$ (He was used as seeding gas in Ref.[5] instead of $H_2$ in the present experiments).

The experimental $S_0$ values reported in Table S8 have been fit with three different functions, and in each case we used the one that returns the smallest $\chi^2$ for that particular set of data. The S-shaped functions tested are the hyperbolic tangent (TANH), the error function (ERF) and the generalized logistic function (LGS), which are given by:

$$S_0^{TANH}(E) = A \cdot \left[1 + tanh\left(\frac{E - E_0}{W}\right)\right] \quad \text{(S9)}$$

$$S_0^{ERF}(E) = \frac{A}{2} \cdot \left[1 + erf\left(\frac{E - E_0}{W}\right)\right] \quad \text{(S10)}$$

$$S_0^{LGS}(E) = A \Big/ \left[1 + \nu \cdot exp\left(-\frac{E - E_0}{W}\right)\right]^{1/\nu} \quad \text{(S11)}$$

The fitting parameters $A$, $W$, $E_0$ and $\nu$ are related to the saturation value, the gradient, the inflection point and the degree of asymmetry of the curves, respectively[96]. The results for Pt(111) have been fitted using the LGS function while for the results for Pt(211) the ERF function was used. The optimized parameters for each set of data are reported in Table S9 and all the results are reported in Figs. S1 and S14 for Pt(211) and Pt(111), respectively.

The agreement between experiments and AIMD simulations with the SRP32-vdW functional is good through the whole energy range on both the surfaces considered. A Stouffer's composite Z-score analysis[95] suggests that there is no statistical evidence that the theoretical reaction probabilities differ from the experimental ones for any of the datasets. This can be argued because the calculated p-value is larger than the typically employed 5% threshold for all the data sets: 0.706 and 0.941 for Pt(111) laser-off and $\nu_1$=1, respectively 0.742 for all Pt(111) data combined, and 0.469 and 0.531 for Pt(211) laser-off and $\nu_1$=1, respectively, and 0.344 for all Pt(211) data combined (see Table S1). In addition, these p-values are all larger than our threshold value ($\alpha$=0.1).

In calculating the p-value for Pt(211), we have not taken into account the agreement between theory and experiment for the lowest $\langle E_i \rangle$. AIMD cannot reliably be used to compute the sticking probability for this collision energy on Pt(211) (for both $v_1$=1 and laser-off conditions), and therefore at those energies the theoretical sticking coefficients cannot be used for a fair comparison with experiments. The reason for this is the large trapping probability (0.025 and 0.014 for laser-off and $v_1$=1, respectively) compared to the reaction probability (see Fig. S1). The mean trapping time on the surface has been estimated using Frenkel's formula[97] to be about 40 ps. In this time frame a molecule can explore the surface and react on defects of the ideal (211) surface (e.g. kinks), thereby increasing the reaction probability. At all other $\langle E_i \rangle$ the trapping probability is lower, and the agreement between theory and experiment is excellent. Note that we are not making an argument for trapping-enhanced reaction on an ideal Pt(211) surface; for this, the adsorption well depth on Pt(211) should be larger, and the dissociation barrier should be smaller. Evidence for trapping mediated reaction for which defects are presumably not needed has been found for $CH_4$ + $IrO_2$(110)[98], for $CH_4$ + Ir(111)[99], and for other light alkanes on Pt(110)x(1x2)[100] and on Ir surfaces[101–103].

Stouffer's test indicates that it is very unlikely that the differences between theory and experiment for all systems combined, and for the conditions at which a rigorous comparison between the AIMD calculations and the experiments are possible, are due to systematic differences between the two, demonstrating that the deviations observed are consistent with statistical fluctuations. Specifically, we compute a p-value close to 0.97 for the hypothesis that under these conditions the AIMD and the experimental data agree. For this particular test, the lowest $\langle E_i \rangle$ laser-off and $v_1$=1 data points for $CHD_3$ + Pt(211) were excluded (due to significant trapping), and the laser-off $CHD_3$ + Ni(111) data taken with $T_n \geq 700$ K were excluded.

To evaluate the quality of our simulations we computed the horizontal distance ($\delta\varepsilon$) in kJ/mol from the AIMD results to the experimental data fit. For Pt(111) (see Fig. S14) the average horizontal distance ($\langle\delta\varepsilon\rangle$) is 2.5 kJ/mol which is smaller than the chemical accuracy criterion we aim for (i.e. 4.2 kJ/mol ≈ 1 kcal/mol). Only three out of eleven AIMD points show $\delta\varepsilon$ > 4.2 kJ/mol. However, for the points sitting at the extremity of the experimental energy range we have to rely on the extrapolation of the fit in order to compute the $\delta\varepsilon$, thereby reducing the reliability of our definition of chemical accuracy. On the Pt(211) surface we have $\langle\delta\varepsilon\rangle$ = 3.4 kJ/mol for the laser-off reaction (again excluding the lowest energy point where the trapping probability is large, see Fig. S1). The $v_1$=1 data could not be included in the analysis for Pt(211) because we do not have enough experimental points to fit a three-parameter S-shape function; however, we note that the AIMD results (excluding the lowest energy point in Fig. S1) fall within the experimental error bars.

Considering all the results for both surfaces, we argue that the SRP32-vdW functional first obtained for $CHD_3$ on Ni(111), allows for the simulation of the $CHD_3$ dissociation on both Pt(111) and Pt(211) with chemical accuracy. The comparison between theoretical results and experiments show a $\langle\delta\varepsilon\rangle$ smaller than 4.2 kJ/mol in all cases. The results show that (i) the SRP functional for $CHD_3$ + Pt(111) is also an SRP functional for $CHD_3$ + Pt(211), and (ii) the SRP functional for $CHD_3$ + Ni(11) is also an SRP functional for $CHD_3$ + Pt(111). The most important result is result (i), as it allows one to bridge a gap between surface science studies on molecules interacting with flat surfaces and the computational modelling of heterogeneous catalysis, where reaction on defects such as steps also has to be considered. Result (ii) also suggests that SRP functionals are transferable among systems in which one and the same molecule interacts with a low index surface of a metal belonging to the same group of the periodic table (both Ni and Pt belong to group X).

According to a classical version of the hole model[104], the sticking probability can be calculated by integrating the fractional number of barriers $N(E)$ over collision energy $E_i$ as:

$$S(E_i) = \int_0^{E_i} N(E')dE'. \quad \text{(S12)}$$

As also argued intensively in Refs.[11] and[32], being able to describe quantitatively different state-selected reaction probability curves suggests that we are accurately describing $N(E)$ and its dependence on the molecular orientation, impact site and surface vibration, and that our model allows us to extract the minimum barrier height with chemical accuracy for the systems addressed.

In addition, the calculations reproduce the experimental vibrational efficacy (i.e., how efficient the vibrational energy is in promoting the reaction) and, according to Polanyi's rule[105], which relates the vibrational efficacy to the dissociating bond length at the TS, this suggests that the SRP32-vdW functional accurately describes the minimum barrier geometry as well for the three systems addressed[11,32].

We argue that the arguments presented in the above two paragraphs and in Refs.[11,32] allow us to extract an accurate value of the minimum barrier height and geometry for methane on Pt(211) and an accurate SRP functional for kinetics simulations even though trapping prevented an accurate comparison between theory and measurements for the lowest $E_i$ for which measurements were performed (see Fig.S1). While it would have been preferable to be able to perform the comparison also for this lowest $E_i$, the extent of the agreement between theory with the SRP functional and experiment for laser-off and initial state-selected reaction at the higher $E_i$ is such that this high level of agreement could not have been reached with a functional underestimating the barrier height by ≥ 1 kcal/mol.

5.2 Reaction site and fraction of CH bond cleavage

The AIMD trajectories on Pt(211) have been analyzed investigating the reaction site and the fraction of CH bond cleavage. Considering the whole energy range, 94% of the reactions occurs in the vicinity of the under-coordinated step edge atoms. This can be seen in Figs. S15 and 3, where the center of mass of the molecules is plotted at the beginning of the trajectory and at the time of the reaction, here defined as the time when the reacting bond is as long as the bond in the TS geometry ($r_{TS}$).

In Fig. S16 the fraction of CH bond cleavage computed for both step and terrace as $p_{CH}^{site} = N_{CH}^{site}/N^{site}$ is reported; here *site* stands for either step or terrace, $N_{CH}^{site}$ is the number of reactive events occurring by CH cleavage, and $N^{site}$ is the total number of reactive events. If the fraction of CH cleavage is either equal to 0 or to 1 the errors ($\sigma_{CH}$) have been calculated using the Louis confidence intervals[106]; in the other cases the error has been calculated as $\sigma_{CH} = \sqrt{p_{CH}^{site} \cdot (1 - p_{CH}^{site})/N^{site}}$. The reaction is statistical for laser-off calculations for which we observe approximately 25% of CH bond cleavage while it is CH bond-selective for $\nu_1$=1 calculations.

## 6. Quantum scattering calculations: comparison of PBE and SRP results for $CHD_3$ + Pt(111)

Jackson and co-workers have developed a fully quantum scattering approach for modelling the dissociative chemisorption of methane on metal surfaces. Based on the reaction path Hamiltonian (RPH) [107], the method treats all molecular degrees of freedom, as well as lattice motion, and has helped to elucidate the origins of the vibrational enhancement, mode-specificity

and the strong variation in $S_0$ with substrate temperature observed for these reactions[42,49,108–111]. In order to understand why the SRP functional provides a better description of these reactions than the commonly-used PBE functional[65,77], we compute $S_0$ for $CHD_3$ incident on Pt(111) using both functionals, and compare the results in detail. We review the essential features of our model here, though full details can be found in recent publications[44,110,111]. The PES and all parameters in the model are computed from first principles using VASP developed at the Institut für Materialphysik of the Universität Wien[74,81,82,112,113]. Interactions between the ionic cores and the electrons are described by fully nonlocal optimized PAW potentials[74,75]. A 5-layer 3×3 supercell with periodic boundary conditions is used to model our system as a slab with a methane coverage of 1/9 ML.

The Hamiltonian for methane dissociation over a rigid metal lattice can be written:

$$H = K + V = -\frac{\hbar^2}{2}\sum_{i=1}^{15}\frac{\partial^2}{\partial x_i^2} + V(x_1, x_2, ..., x_{15}), \qquad \text{(S13)}$$

where the $x_i$ are the 15 mass-weighted Cartesian coordinates of the $CH_4$ nuclei. To construct our PES (V) we first locate the minimum energy path (MEP) from the TS to the reactant and product configurations using the CI-NEB method[114,115]. The distance along the MEP is s, where $(ds)^2 = \sum_{i=1}^{9}(dx_i)^2$, and s = 0 at the TS. We denote the energy along the MEP as $V_0(s)$. In Fig. S17 we plot $V_0(s)$ for both the PBE and SRP functional. Jackson and co-workers independently calculated that the inclusion of van der Waals forces in the SRP functional gives a physisorption well depth of 20.7 kJ/mol, which is in agreement with that reported in Sec 3.3. The barrier heights for the two functionals are very similar, as are the TS geometries, though the length of the dissociating bond at the TS is somewhat larger for the SRP functional: 1.56 Å *vs.* 1.52 Å for PBE.

At each image along the MEP we compute and diagonalize the force-projected Hessian to find the 14 normal vibrational coordinates $Q_k$ and corresponding frequencies $\omega_k(s)$ that describe

displacements orthogonal to the reaction path at s, in the harmonic approximation. Our PES, in the reaction path coordinates s and $\{Q_k\}$, is thus:

$$V = V_0(s) + \sum_{k=1}^{8} \frac{1}{2} \omega_k^2(s) Q_k^2. \quad \text{(S14)}$$

For $CHD_3$ dissociation on Pt(111) there are four unique molecular orientations at the TS, shown in Fig. S18. For molecules in the $\nu_1$ state, the CH cleavage configuration is responsible for most of the dissociative sticking, particularly at lower energies. For ground state molecules, the CH cleavage configuration is the most important of the four, except at very high energies when all four contribute equally to reaction (a CH cleavage fraction of 0.25). We thus focus our attention here on the CH cleavage configuration, though when we compute $S_0$, contributions from all four configurations are included.

In Fig. S19 we plot some of the normal mode energies $\hbar\omega_q(s)$ along the reaction path for the CH scission case of Fig. S18, using both functionals. When $CHD_3$ is far above the surface (large negative s) there are nine internal bending and stretching modes with nonzero frequency, and 5 modes with zero frequency, corresponding to rotation of the molecule and translation parallel to the surface. The MEP is symmetric with respect to reflection through a plane perpendicular to the surface and including the C and H atoms. The 14 normal modes are thus either symmetric or antisymmetric with respect to this reflection. This is important, as energy can only flow between modes of the same symmetry, and the 6 symmetric modes corresponding to internal vibration dominate the reaction dynamics for both ground state and excited molecules. We thus include only the 6 modes in Fig. S19, using the traditional labels $\nu_1 - \nu_6$. The normal modes computed using the two functionals are similar, though there is a slightly larger softening of the reactive CH stretch for the SRP functional.

We write our total molecular wave function, in reaction path coordinates, as:

$$\Psi(t) = \sum_{\mathbf{n}} \chi_{\mathbf{n}}(s;t)\, \Phi_{\mathbf{n}}\left(\{Q_k\};s\right), \tag{S15}$$

where the $\Phi_n$ are products of harmonic oscillator eigenfunctions that depend parametrically on s, and the vector **n** labelling the vibrational states corresponds to a set of quantum numbers $n_k$. The equations of motion for the wave packets, $\chi_{\mathbf{n}}(s; t)$, are of the form[49]:

$$i\hbar \frac{\partial \chi_{\mathbf{n}}(s;t)}{\partial t} = \left[\frac{1}{2} p_s^2 + V_0(s) + \sum_{k=1}^{14} \hbar\omega_k(s)\left(n_k + \frac{1}{2}\right)\right]\chi_{\mathbf{n}}(s;t) + \sum_{\mathbf{n}'} F_{\mathbf{n}\mathbf{n}'}\chi_{\mathbf{n}'}(s;t). \tag{S16}$$

The wave packets evolve on vibrationally adiabatic potential energy surfaces for each vibrational state **n**, and the operators $F_{\mathbf{nn}'}$ couple states of the same symmetry. The $F_{\mathbf{nn}'}$ are proportional to the vibrationally nonadiabatic couplings, $B_{q,k}(s)$, computed from the normal mode eigenvectors[49,107]. Because of the parametric dependence of the $\Phi_{\mathbf{n}}$ on s, the $F_{\mathbf{nn}'}$ also contain momentum and kinetic energy operators[49]. Thus, curve crossing (transitions between vibrationally adiabatic states) becomes more probable at higher velocities, as well as for larger values of the coupling. The sums over **n** in Eqs. (S15) and (S16) include the vibrationally adiabatic ground state and all states with either one or two vibrational quanta excited. Detailed expressions for the final equations of motion can be found in a recent publication[44]. For a given initial vibrational state, $\mathbf{n_0}$, standard techniques are used to evolve the wave packets of Eq. (S16) and to energy-analyze the reactive flux [42,49] The result is the rigid-lattice reaction probability, $P_0(E_t, \mathbf{n_0})$, for collision at the minimum barrier site. The rotational orientation of the molecule has been allowed to evolve adiabatically.

In Fig. S20 we plot the couplings, $B_{q,k}(s)$, for the CH cleavage configuration, using both functionals. They peak at the avoided crossings of Fig. S19, where transitions can occur between different vibrationally adiabatic states. These couplings are responsible for the large enhancement in reactivity when the molecule is vibrationally excited. For example, a molecule initially in the $\nu_1$ state can transition to the $\nu_4$ state at the avoided crossing around s = -1.3 amu$^{½}$ Å (see Fig. S19),

then to the $\nu_2$, then the $\nu_5$, and so on. With each transition, excess vibrational energy is converted into motion along the reaction path, corresponding to bond breaking at the TS. The SRP couplings are a bit larger for the important $\nu_1$ to $\nu_4$, and $\nu_4$ to $\nu_2$ transitions, but otherwise they are similar. However, if we look more closely further out in the entrance channel, Fig. S21, we see that the SRP functional gives larger couplings where inclusion of van der Waals forces leads to a stronger interaction of the metal with the molecule. While small, these entrance channel couplings can mix near-degenerate states.

Similarly, we find that the so-called curvature couplings, $B_{q,15}(s)$, are similar for the PBE and SRP functionals in the curve-crossing region, where they are largest. These functions couple the ground state to the first excited vibrational states, and are mostly responsible for a decrease in the ground state reaction probability at higher energy, due to vibrational excitation of the incoming molecule. Again, if we look in the region of the attractive well, Fig. S22, we see that the inclusion of van der Waals forces in the SRP functional leads to a larger coupling. We note that the curvature couplings in the region of the avoided crossings (not shown) are about an order of magnitude larger.

In Fig. S3 we plot $P_0$, the rigid-lattice single-site reaction probability for molecules in either the ground state or the $\nu_1$=1 excited state. For the SRP case ("SRP $V_0$ + SRP coupling") we see that molecules in the $\nu_1$=1 state are much more reactive at lower energies than for the PBE case ("PBE $V_0$ + PBE coupling"). This may be due to the slightly larger couplings of Figs. S19 and S20, and/or larger transition probabilities arising from larger molecular velocities in the crossing region, due to the van der Waals attractive well. To disentangle the two effects, we consider two other cases in Fig. S3: the PBE couplings but using $V_0(s)$ from the SRP calculations, and the SRP couplings with $V_0(s)$ from the PBE calculations. For molecules in the $\nu_1$=1 state, it is clear that the

inclusion of the attractive well can enhance the coupling between vibrational states that makes vibrationally excited molecules more reactive. For molecules in the ground state, we see similar behaviour. The SRP functional leads to increased vibrational excitation of incoming molecules, lowering the value of the ground state reactivity near saturation. However, both the modified couplings and the increased molecular velocity appear to be important.

To compute $S_0$ we average $P_0$ over all other surface impact sites, correct the rotational treatment, and include the effects of lattice motion. Motion along X and Y should be slow on collision timescales, given our normal incidence conditions and high collision energies, and AIMD studies confirm this sudden behaviour[5,109]. Assuming that there is no steering of the incident methane along X and Y, and that most reactive trajectories are close to the MEP, we average $P_0$ over all impact sites in the surface unit cell, using the following approximation to estimate $P_0$ for impact at a site (X,Y) away from the minimum barrier site:

$$P_0\left(E_i, \mathbf{n_0}; X, Y\right) \approx P_0\left(E_i - \Delta V, \mathbf{n_0}\right). \quad \text{(S17)}$$

$\Delta$V(X,Y) is the increase in barrier height at (X, Y) relative to the minimum barrier site. We can approximate this using the normal modes, or compute it directly using DFT. AIMD also suggests that the rotational behaviour might be closer to sudden at high collision energies[5,109], while it should be closer to adiabatic at lower incident energies. We use an approach similar to Eq. (S17) to estimate $S_0$ in the sudden limit[109], and define our final $S_0$ as a linear combination of these two limits, such that the behaviour is adiabatic at lower incident energies and sudden at higher incident energies [111]. Finally, to introduce the effects of lattice motion we average $P_0$ over all displacements and momenta normal to the surface of the Pt atom over which the methane dissociates[89,116]. The momentum of this atom determines the relative collision velocity, and the displacements can

significantly change the barrier height. A Debye model is used to describe the motion of this Pt atom[111]. Results for all 4 molecular configurations must then be averaged.

In Fig. S2 we plot both SRP and PBE results for the dissociative sticking of $CHD_3$ molecules in the ground state and several singly-excited stretch and bend states. We see that the overall effect of using the SRP functional is to increase the efficacy of vibrational motion for promoting reaction. This arises both from an increase in $S_0$ for excited states, and a somewhat smaller $S_0$ for ground state molecules at higher energy. For molecules in the $\nu_1$ CH stretch state, we have shown that this is due primarily to the inclusion of the van der Waals attractive well. For the CD stretch states, $\nu_2$ and $\nu_4$, the effect is even larger, and the increased couplings in the region of the attractive well also play a role.

**7. Implications for simulating heterogeneous catalysis.**

The transferability of SRP functionals shown here for dissociative chemisorption of a molecule on a low-index, flat surface to a stepped surface points to a promising approach for accurately simulating rates of heterogeneously catalysed reactions over metal nanoparticles. In this approach, one would use the finding that usually only a few states (transition states, or states describing adsorbed reactants, adsorbed reaction intermediates, or adsorbed products) exhibit a large degree of rate control[117]. Only for these states should it be necessary to determine the molecule-metal surface interaction energy accurately[117]. Of these states, accurate calculations of the transition states should be most important, as molecular adsorption energies are reasonably accessible through experiments using single crystal adsorption calorimetry and thermal desorption spectroscopy[118,119]. It should be possible to fit a semi-empirical functional with an expression similar to that of Eq.1 to a molecule or reaction intermediate adsorbed on a low index metal surface either using existing experimental information, or in a procedure involving a new

adsorption experiment. We argue that the transferability observed in the present work for transition states then suggests that the semi-empirical functional determined in this fashion should also accurately predict adsorption at surface defects, such as steps, edges, kinks and corners. Strong supporting evidence comes from recent work by Sautet and co-workers which showed that adsorption energies of OH and OOH on Pt[120] and other transition metal[121] surfaces depends linearly on the generalized coordination number of the surface atom these species adsorb to, and the finding that, based on these relations, theory is able to correctly predict that specific stepped Pt surfaces are more active for oxygen reduction than the Pt(111) surface[122].

The reaction studied in the present work is an important representative of a class of structure sensitive reactions in which the bond broken is a single σ-type bond (e.g., a CH or single CC bond)[123]. In the transition state of such reactions, the dissociating molecule usually sits on top of a surface atom[123] (a "top site" if the reaction occurs on a low index surface). Usually, the reaction barrier is lowered over surface atoms of lower coordination number[123] (surrounded by fewer nearest neighbour metal atoms), for instance over surface atoms at the top edge of a step, as observed here for $CHD_3$ + Pt(211). The implication of our present work and earlier work on transferability among metal facets[33] is that one can use an SRP functional developed for the reaction on a low index surface to accurately compute barrier heights for the molecule's dissociation over surface atoms occurring in other low index facets and at surface line and point defects with lower coordination numbers of surface atoms. The derived barrier heights can then be used in kinetics simulations of the overall heterogeneously catalysed reaction as it occurs over a metal nanoparticle exhibiting specific facets, line defects, and point defects. We argue that the rates calculated in this manner should be more accurate than rates calculated on the basis of standard density functionals (non-empirical functionals based on constraints, or conventional semi-empirical functions fitted to a range of chemical properties and/or materials properties[124]).

The above argument that rates over defected surfaces computed from SRP functionals accurately describe transition state energies on flat surfaces also has a basis in the recent work of Sautet and co-workers, and the so-called transition state scaling relationships. As noted above, it

is already possible with standard functionals to predict which Pt crystal surface (with atoms located at defects possessing specific generalized coordination numbers) is most active for a specific reaction (oxygen reduction[122]). The adsorption energies of involved reactant molecules depend linearly on the generalized coordination number[120]. In turn, transition state energies usually scale linearly with the adsorption energies of reactants (the transition state scaling relationship)[125,126]. The above suggests that transition state energies should scale linearly with generalized coordination numbers, and that if the off-set of the linear relationship is accurately determined (by determining the transition state energy for the flat surface) it should be possible to accurately determine the transition state energy for other generalized coordination numbers (on stepped surfaces) accurately as well.

Another class of structure-sensitive reactions, in which a double or triple π-bond breaks in the molecule, may present a greater challenge to transferability. Examples of such reactions are CO and $N_2$ bond breaking, where an additional requirement of the transition state (additional to presenting surface atoms with lower coordination number) is that the reaction site is able to coordinate many surface atoms to the dissociating molecule, to facilitate the breaking of a strong double or triple bond[123]. A well-known example concerns ammonia production over Ru particles, in which the rate limiting step is $N_2$ bond breaking. Nørskov and co-workers have established that this reaction is accelerated by so-called B5-sites, in which the dissociation molecule is co-ordinated by 5 surface atoms[127]. Incidentally, such B5 sites are also present at the Pt(211) steps, and, more generally, at surfaces where hcp(0001) terraces or fcc(111) terraces are connected by (100)-type steps (see Ref.[128] and figure 1 therein). Our present results show that on Pt(211) methane reacts at the step edge sites that are part of these B5 sites. The additional requirement of providing a higher coordination to the dissociating molecule might be perceived to present a greater challenge to the transferability of SRP functionals. However, we emphasize that the difference between the two broad classes of structure sensitive reactions is gradual. In the case we have looked at, the SRP functional is able to accurately describe the effect of changing the coordination number of the surface atom above which dissociation occurs. In the case of double

or triple bond breaking, the SRP functional should additionally be able to describe the effect of the coordination to additional surface atoms for transferability to hold. While the accuracy with which this can be done has yet to be established, we argue that a similar approach to that taken here for $CHD_3$ + Pt(111) and Pt(211) and based on an SRP functional for the flat surface should be better than simply taking a constraint-based or conventional semi-empirical functional to obtain reaction barrier heights on facets and at surface defect reaction sites. In this respect, it is encouraging that the transition scaling relations accurately describe the relation between the transition state energies of $N_2$, CO, and NO on (211) fcc surfaces and the adsorption energies of these molecules at the upper terrace hcp sites[129].

Finally, the question might arise whether the approach we advocate would be sensible if, for example, simple bond breaking of a reactant molecule dominates the reaction at steps, while the breaking of this bond is preceded by reaction with another reactant on the terraces. A practical example is the initiation of Fischer-Tropsch synthesis over ≈ 4.6 nm Co nanoparticles, which expose 15% under-coordinated sites, which are mostly step edges of A- and B-type capable of direct CO-dissociation[130]. For this example, Westrate et al.[130] concluded that one can reasonably assume that direct CO dissociation at the undercoordinated sites is the primary mechanism for the initiation of the Fischer-Tropsch reaction, even though the reaction on the facets might proceed through a mechanism in which CO is hydrogenated prior to CO bond breaking. Therefore, the development of an SRP functional for dissociative chemisorption of the CO molecule on a terrace and its application to the reaction of the same molecule at steps might help to accurately describe an overall catalysed reaction if this reaction is dominated by the steps, even though the rate limiting step, and indeed the mechanism of the catalysed reaction, could be different on the flat surfaces making up the facets. Here, by the overall catalysed process we mean the initiation of a Fischer-Tropsch synthesis reaction, and not necessarily the complete Fischer-Tropsch reaction making higher hydrocarbons. Note that one can determine whether line defects (such as steps) or point defects (such as kinks) dominate the rate of a catalysed process over catalyst particles by determining the degree of structure reactivity parameter $\alpha$, which describes the dependence of the

rate on the catalyst particle diameter $d$[131]. For example, $\alpha = 1$ describes a process where the rate is dominated by line defects, and this value was found to accurately describe the rate of steam reforming over supported Pt nanoparticles [132].

The above finding of $\alpha = 1$ for steam reforming over Pt nanoparticles is only one reason that steam reforming over Pt nanoparticles should constitute an ideal test case for our SRP density functional for methane interacting with Pt particles. Wei and Iglesia also found that steam reforming rates over Pt particles were exclusively limited by the first CH-bond cleavage [132]. Additionally, they found that steam reforming over supported Pt nanoparticles proceeds over essentially uncovered catalyst particles, and that support effects are indirect (they are described fully by how the support affects the shape of the catalyst particles).

Our approach is useful for getting accurate transition states for elementary dissociation reactions of molecules that are stable in the gas phase, and therefore useful for simulating heterogeneous catalysis if such reactions play an important role in the mechanism of the catalysed reaction. Examples of such reactions are dissociative chemisorption of methane in steam reforming[132,133], of water in the water gas shift reaction[134], of $N_2$ in ammonia production[127,135], and of CO in many realizations of the Fischer-Tropsch process[136]. It is less useful if the rate limiting step is, for instance, the hydrogenation of an already adsorbed reaction intermediate, as is the case for the overall Fischer-Tropsch synthesis reaction over supported Fe nanoparticles[137]. Catalysed reactions with complex reaction mechanisms (such as hydrogenation of olefins on supported Pd catalysts involving sub-surface hydrogen[138] certainly exist for which the present approach will be of little help. Nevertheless, our new approach is likely to provide valuable input for catalysed reactions in which the overall rate is dominated by simple dissociation reactions of stable molecules.

## Supporting Tables

**Table S1.** Stouffer's composite Z-scores and corresponding p-values for the various data sets considered. Note that for the Pt(211) surface and laser-off conditions the lowest energy point has not been included in the calculation of the Z-score.

| Surface | Conditions | k | Composite Z-score | p-value |
|---|---|---|---|---|
| Pt(111) | laser-off | 6 | 0.377 | 0.706 |
| Pt(111) | $\nu_1$=1 | 5 | 0.074 | 0.941 |
| Pt(111) | all | 11 | 0.329 | 0.742 |
| Pt(211) | laser-off | 5 | -0.724 | 0.469 |
| Pt(211) | $\nu_1$=1 | 2 | -0.626 | 0.531 |
| Pt(211) | All | 7 | -0.946 | 0.344 |
| All | all | 26 | 0.041 | 0.968 |

**Table S2.** Molecular beam parameters that characterize the experimental $CHD_3$ velocity distributions used in the calculations. $v_0$ and $\alpha$ were determined through time-of-flight measurements, as described in Sec. 1.3.1.

$CHD_3$ on Pt(111), laser-off

| Nozzle temperature, $T_n$ (K) | Translational energy $\langle E_i \rangle$ (kJ/mol) | Stream velocity $v_0$ (m/s) | Width parameter $\alpha$ (m/s) |
|---|---|---|---|
| 400 | 81.7 | 2899 | 216 |
| 450 | 89.3 | 3026 | 246 |
| 500 | 97.4 | 3157 | 270 |
| 550 | 102.5 | 3231 | 299 |
| 600 | 111.9 | 3369 | 333 |
| 650 | 120.1 | 3483 | 367 |

$CHD_3$ on Pt(111), laser-on

| Nozzle temperature, $T_n$ (K) | Translational energy $\langle E_i \rangle$ (kJ/mol) | Stream velocity $v_0$ (m/s) | Width parameter $\alpha$ (m/s) |
|---|---|---|---|
| 298 | 60.7 | 2512 | 131 |
| 350 | 71.4 | 2723 | 149 |
| 400 | 81.9 | 2913 | 176 |
| 450 | 92.2 | 3089 | 198 |
| 500 | 104.6 | 3284 | 232 |

$CHD_3$ on Pt(211), laser-on and laser-off

| Nozzle temperature, $T_n$ (K) | Translational energy $\langle E_i \rangle$ (kJ/mol) | Stream velocity $v_0$ (m/s) | Width parameter $\alpha$ (m/s) |
|---|---|---|---|
| 298 | 58.2 | 2454 | 159 |
| 350 | 69.2 | 2671 | 194 |
| 400 | 79.5 | 2856 | 232 |
| 450 | 92.5 | 3076 | 266 |
| 500 | 96.8 | 3151 | 257 |
| 550 | 107.9 | 3321 | 288 |

**Table S3.** Transition state energies calculated with VASP and QE for the various functionals and implementations of the vdW correlation: the spin-polarized extension of the originally proposed spin-unpolarized vdW correlation (*), as implemented in VASP, and the more rigorously derived spin-polarized vdW correlation (**), as implemented in QE.

| DFT code | Functional | $E_b$ (kJ/mol) |
|---|---|---|
| VASP | PBE | 92.5 |
| VASP | vdW-DF * | 121.7 |
| VASP | SRP32-vdW * | 101.8 |
| QE | PBE | 92.7 |
| QE | vdW-DF ** | 121.1 |
| QE | SRP32-vdW ** | 100.8 |

**Table S4.** Convergence test for $CHD_3$ on Pt(111) investigating number of layers, unit cell size (Nx,Ny), plane wave cut off energy and k-points sampling in both directions in momentum space along the surface. In the table the energy of the TS ($E_b^{13Å}$) and the difference ΔE with the best converged set up (last line) are reported. The set up chosen for the AIMD simulations is reported in the first line. All the results are reported for the SRP32-vdW functional. Note: 1 eV = 96.49 kJ/mol.

| | | | | | SRP32-vdW | |
|---|---|---|---|---|---|---|
| Layers | Nx | Ny | cut off (eV) | k-points | $E_b^{13Å}$ ( eV ) | ΔE (meV) |
| 5 | 3 | 3 | 350 | 4 | 0.856 | -5 |
| 5 | 3 | 3 | 350 | 3 | 0.804 | -57 |
| 5 | 3 | 3 | 350 | 4 | 0.856 | -5 |
| 5 | 3 | 3 | 350 | 8 | 0.868 | 7 |
| 5 | 3 | 3 | 350 | 11 | 0.868 | 7 |
| 5 | 3 | 3 | 300 | 4 | 0.832 | -29 |
| 5 | 3 | 3 | 350 | 4 | 0.856 | -5 |
| 5 | 3 | 3 | 400 | 4 | 0.861 | 0 |
| 5 | 3 | 3 | 500 | 4 | 0.862 | 1 |
| 4 | 3 | 3 | 350 | 4 | 0.934 | 73 |
| 5 | 3 | 3 | 350 | 4 | 0.856 | -5 |
| 6 | 3 | 3 | 350 | 4 | 0.855 | -6 |
| 5 | 2 | 2 | 350 | 4 | 0.933 | 72 |
| 5 | 3 | 3 | 350 | 4 | 0.856 | -5 |
| 5 | 4 | 4 | 350 | 4 | 0.852 | -9 |
| 6 | 2 | 2 | 350 | 4 | 0.918 | 57 |
| 6 | 3 | 3 | 350 | 4 | 0.855 | -6 |
| 6 | 4 | 4 | 350 | 4 | 0.861 | 0 |

**Table S5**. Convergence test for $CHD_3$ on Pt(211) investigating number of layers, unit cell size (Nx,Ny), plane wave cut off energy and k-points sampling in both directions in momentum space along the surface. In the table the energy of the TS ($E_b^{13Å}$) and the difference ΔE with the best converged set up (last line) are reported. The set up chosen for the AIMD simulations is reported in the first line. All the results are reported for the SRP32-vdW functional. Note: 1 eV = 96.49 kJ/mol.

| | | | | | SRP32-vdW | |
|---|---|---|---|---|---|---|
| Layers | Nx | Ny | cut off (eV) | k-points | $E_b^{13Å}$ (eV) | ΔE (meV) |
| 4 | 1 | 3 | 350 | 4 | 0.566 | -7 |
| 5 | 1 | 3 | 350 | 4 | 0.592 | 19 |
| 6 | 1 | 3 | 350 | 4 | 0.582 | 9 |
| 4 | 1 | 2 | 350 | 4 | 0.599 | 26 |
| 4 | 1 | 3 | 350 | 4 | 0.566 | -7 |
| 4 | 1 | 4 | 350 | 4 | 0.558 | -15 |
| 4 | 2 | 2 | 350 | 4 | 0.559 | -14 |
| 4 | 2 | 3 | 350 | 4 | 0.543 | -30 |
| 4 | 2 | 4 | 350 | 4 | 0.537 | -36 |
| 5 | 1 | 2 | 350 | 4 | 0.587 | 14 |
| 5 | 1 | 3 | 350 | 4 | 0.592 | 19 |
| 5 | 1 | 4 | 350 | 4 | 0.586 | 13 |
| 5 | 2 | 2 | 350 | 4 | 0.559 | -14 |
| 5 | 2 | 3 | 350 | 4 | 0.571 | -2 |
| 5 | 2 | 4 | 350 | 4 | 0.566 | -7 |
| 4 | 1 | 3 | 300 | 4 | 0.541 | -32 |
| 4 | 1 | 3 | 350 | 4 | 0.566 | -7 |
| 4 | 1 | 3 | 400 | 4 | 0.572 | -1 |
| 4 | 1 | 3 | 500 | 4 | 0.573 | 0 |
| 4 | 1 | 3 | 350 | 3 | 0.539 | -34 |
| 4 | 1 | 3 | 350 | 4 | 0.566 | -7 |
| 4 | 1 | 3 | 350 | 8 | 0.549 | -24 |
| 4 | 1 | 3 | 350 | 11 | 0.549 | -24 |
| 5 | 2 | 4 | 500 | 8 | 0.573 | 0 |

**Table S6.** Minimum barrier computed with the SRP32-vdW functionals. From top to bottom are reported: the barrier using 13 Å of vacuum ($E_b^{13\text{Å}}$), the barrier using 30 Å of vacuum ($E_b^{30\text{Å}}$), the residual energy ($E_R$), the effective barrier in the AIMD simulations ($E_b^e$) and the difference between $E_b^{30\text{Å}}$ and $E_b^e$. See text for further details. Results for Ni(111) are reported from previous work [11].

| | | Pt(111) | Pt(211) | Ni(111) |
|---|---|---|---|---|
| $E_b^{13\text{Å}}$ | (kJ/mol) | 82.6 | 54.6 | 101.8 |
| $E_b^{30\text{Å}}$ | (kJ/mol) | 77.7 | 51.4 | 96.5 |
| $E_R$ | (kJ/mol) | 4.0 | 2.0 | 3.9 |
| $E_b^e$ | (kJ/mol) | 78.6 | 52.6 | 97.9 |
| $E_b^e - E_b^{30\text{Å}}$ | (kJ/mol) | 1.0 | 1.2 | 1.4 |

**Table S7.** Largest adsorption well for the systems studied corrected by the residual energy ($E^c_{ads}$) (see text for details), and the height of the carbon atom above the surface ($Z_C$). The experimental values for the adsorption energy have been taken from Refs.[93] and[139,140] for Pt(111) and Ni(111), respectively.

| System | Largest $E^c_{ads}$ (kJ/mol) | $Z_C$ (Å) | Experimental adsorption energy (kJ/mol) |
|---|---|---|---|
| Pt(111) | 21.9 | 3.648 | 18 |
| Pt(211) | 24.8 | 3.380 | - |
| Ni(111) | 18.9 | 3.546 | 12 |

**Table S8**. Experimental and AIMD results compared. The average beam energy $\langle E_i \rangle$ is reported together with the number of trajectories used in the simulations ($N_i$), the experimental zero-coverage reaction probability $S_0$ and the AIMD reaction probability $p_i$ with the related errors ($\sigma$ and $\sigma_i$, respectively).

| $\langle E_i \rangle$ (kJ/mol) | $N_i$ | Exp. $S_0$ | Exp. $\sigma$ | AIMD $p_i$ | AIMD $\sigma_i$ |
|---|---|---|---|---|---|
| Pt(111) - laser-off | | | | | |
| 81.7 | 1000 | 0.023 | 0.005 | 0.023 | 0.005 |
| 89.3 | 1000 | 0.036 | 0.005 | 0.030 | 0.005 |
| 97.4 | 500 | 0.054 | 0.005 | 0.060 | 0.011 |
| 102.5 | 500 | 0.071 | 0.006 | 0.086 | 0.013 |
| 111.9 | 500 | 0.100 | 0.008 | 0.094 | 0.013 |
| 120.1 | 500 | 0.130 | 0.010 | 0.140 | 0.016 |
| Pt(111) - $\nu_1$=1 | | | | | |
| 60.7 | 1000 | 0.032 | 0.007 | 0.025 | 0.005 |
| 71.4 | 500 | 0.047 | 0.008 | 0.048 | 0.010 |
| 81.9 | 500 | 0.069 | 0.016 | 0.066 | 0.011 |
| 92.2 | 500 | 0.078 | 0.016 | 0.084 | 0.012 |
| 104.6 | 500 | 0.113 | 0.029 | 0.138 | 0.015 |
| Pt(211) - laser-off | | | | | |
| 58.2 | 1000 | 0.016 | 0.005 | 0.006 | 0.002 |
| 69.2 | 1000 | 0.027 | 0.005 | 0.019 | 0.004 |
| 79.5 | 500 | 0.043 | 0.005 | 0.040 | 0.009 |
| 92.5 | 500 | 0.061 | 0.005 | 0.058 | 0.011 |
| 96.8 | 500 | 0.075 | 0.005 | 0.070 | 0.011 |
| 107.9 | 500 | 0.094 | 0.005 | 0.102 | 0.014 |
| Pt(211) - $\nu_1$=1 | | | | | |
| 58.2 | 500 | 0.068 | 0.020 | 0.030 | 0.008 |
| 69.2 | 500 | 0.083 | 0.012 | 0.076 | 0.012 |
| 79.5 | 500 | 0.083 | 0.030 | 0.068 | 0.011 |

**Table S9.** Types of function and parameters used to fit the experimental $S_0$ data.

| | | | Parameters | | | |
|---|---|---|---|---|---|---|
| Surface | State | Function | $A$ | $E_0$ (kJ/mol) | $W$ (kJ/mol) | $v$ |
| Pt(111) | laser-off | LGS | 0.28 | 118.04 | 23.01 | 0.48 |
| Pt(111) | $v_1$=1 | LGS | 1.30 | 203.31 | 109.97 | 4e-07 |
| Pt(211) | laser-off | ERF | 0.170 | 102.98 | 48.01 | - |

**Supporting Figures**

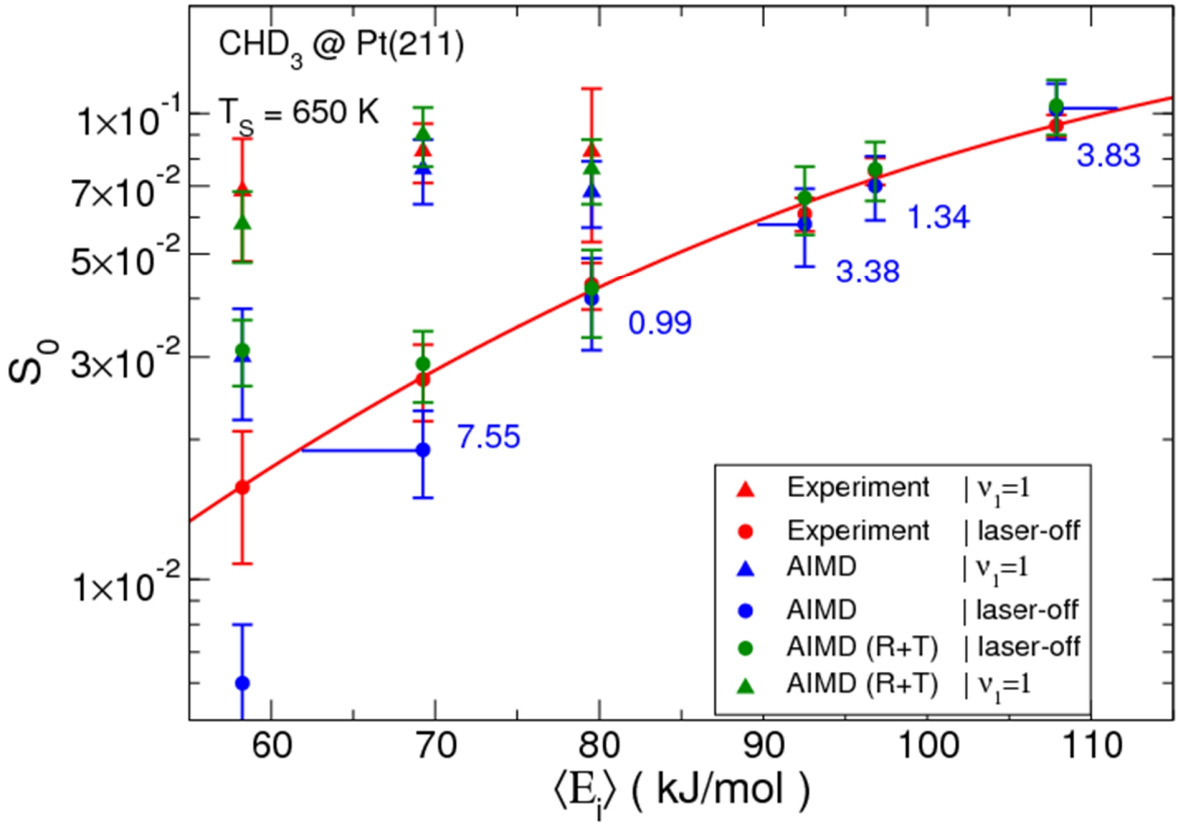


**Fig. S1.** Experimental and AIMD results (red and blue, respectively) for $CHD_3$ on Pt(211). The AIMD results computed considering the trapped trajectories as reacted are reported in green. The distances from the AIMD points to the fit (in kJ/mol) are reported in blue.

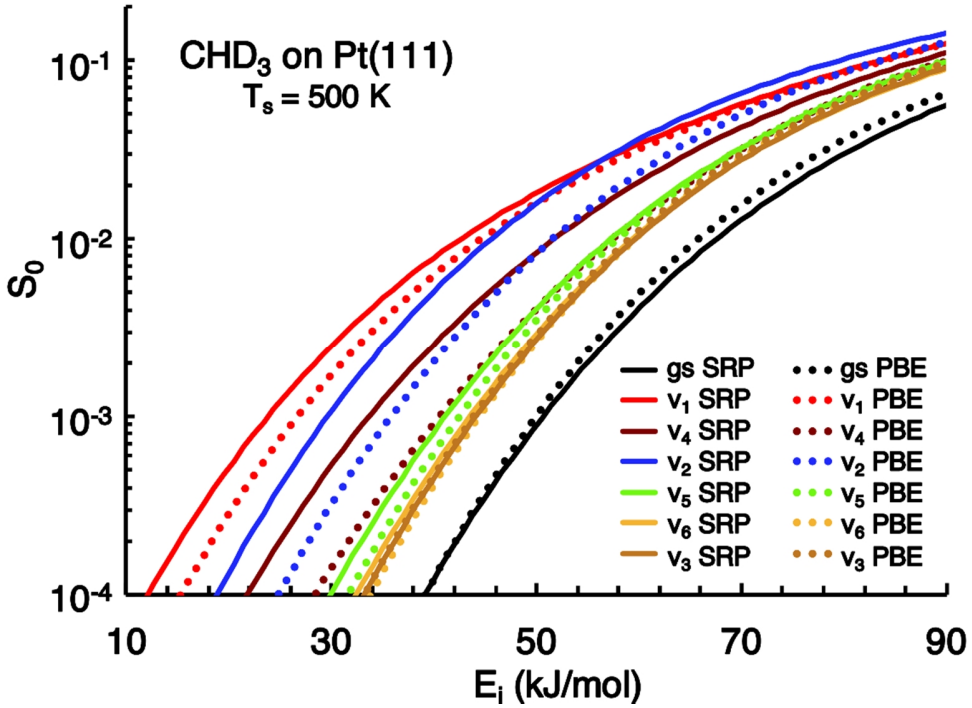


**Fig. S2.** Dissociative sticking probabilities, $S_0(E_i)$, for the dissociative chemisorption of $CHD_3$ on Pt(111), for a surface temperature of 500 K. The molecules are initially in the ground vibrational state, or one of the single-quantum vibrational states indicated.

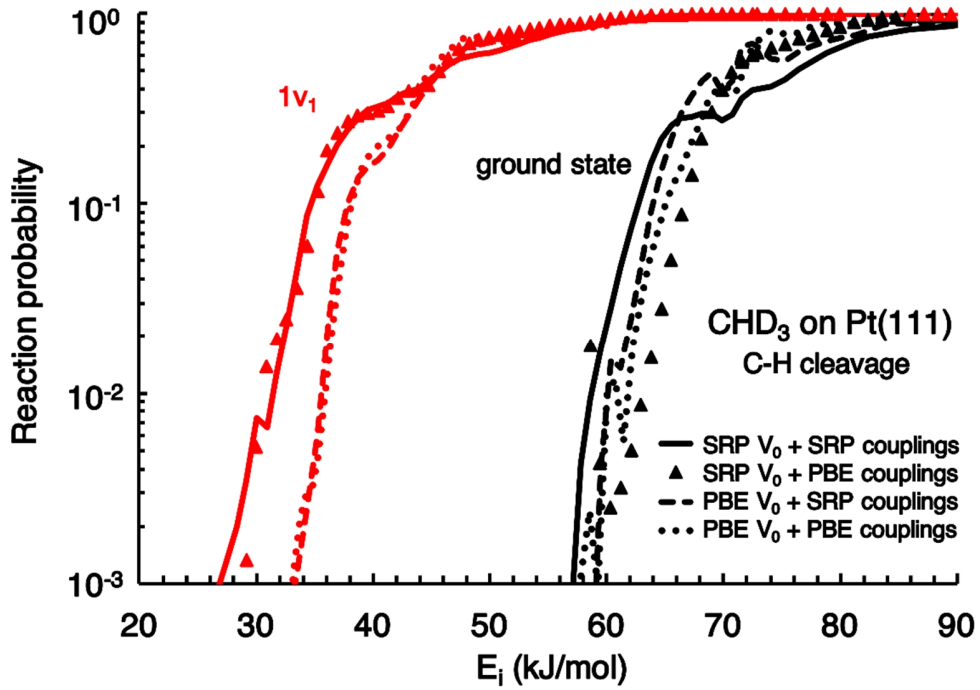


**Fig. S3.** Rigid-surface single-site reaction probabilities, $P_0(E_i)$, for the CH cleavage configuration. The molecules are initially in the ground vibrational state or the $v_1$=1 excited state. Four combinations of coupling and MEPs are included, as discussed in the text.

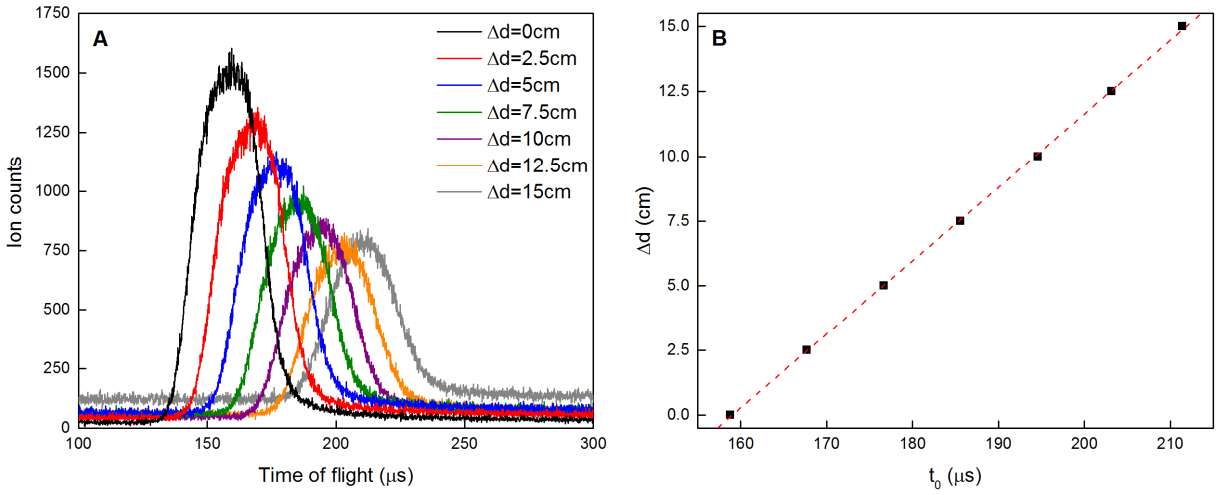


**Fig. S4.** Panel A: Time-of-flight profiles recorded for the 1.5% $CHD_3$ in $H_2$ mixture used for the King and Wells experiments at a nozzle temperature of 400 K. Panel B: Δd *vs* $t_0$ obtained by fitting the time-of-flight profiles. The dashed line shows a fit to the data, the gradient of which corresponds to the velocity of the molecular beam.

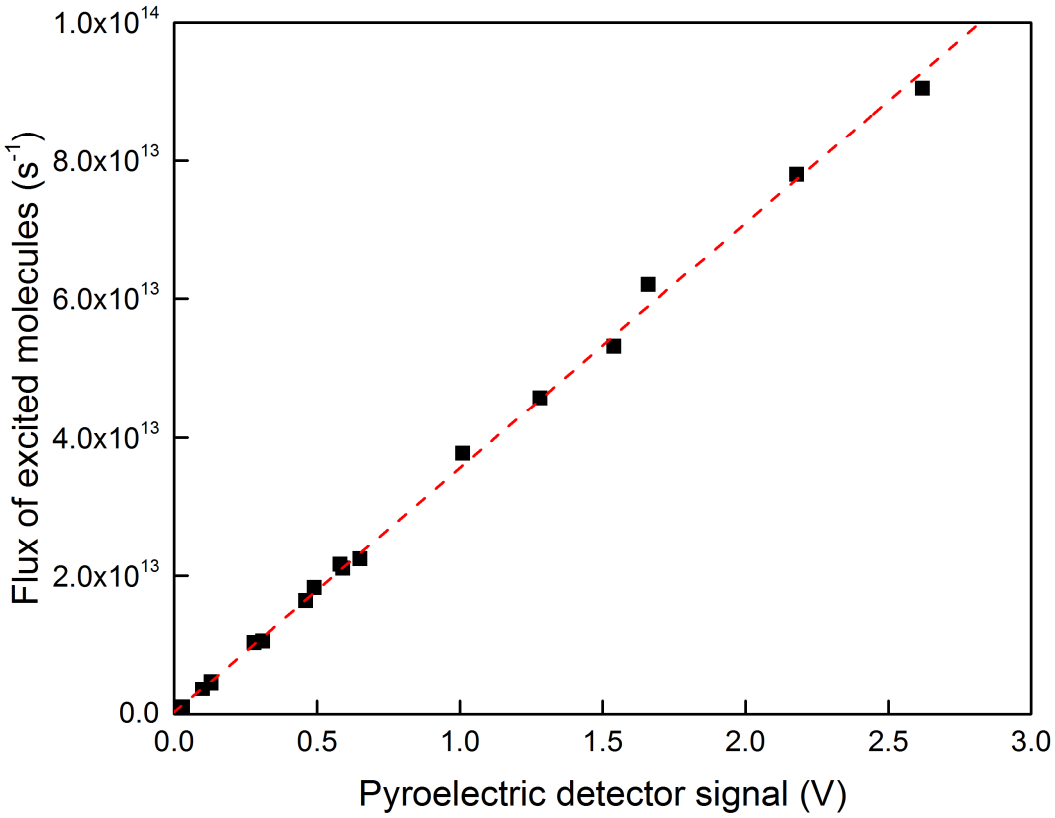


**Fig. S5.** The pyroelectric detector calibration, showing that the measured signal is proportional to the flux of excited molecules into the UHV chamber. The dashed red line is a fit to the data, which was used to determine the flux of excited $CHD_3$, and $f_{exc}$ for the measurements here.

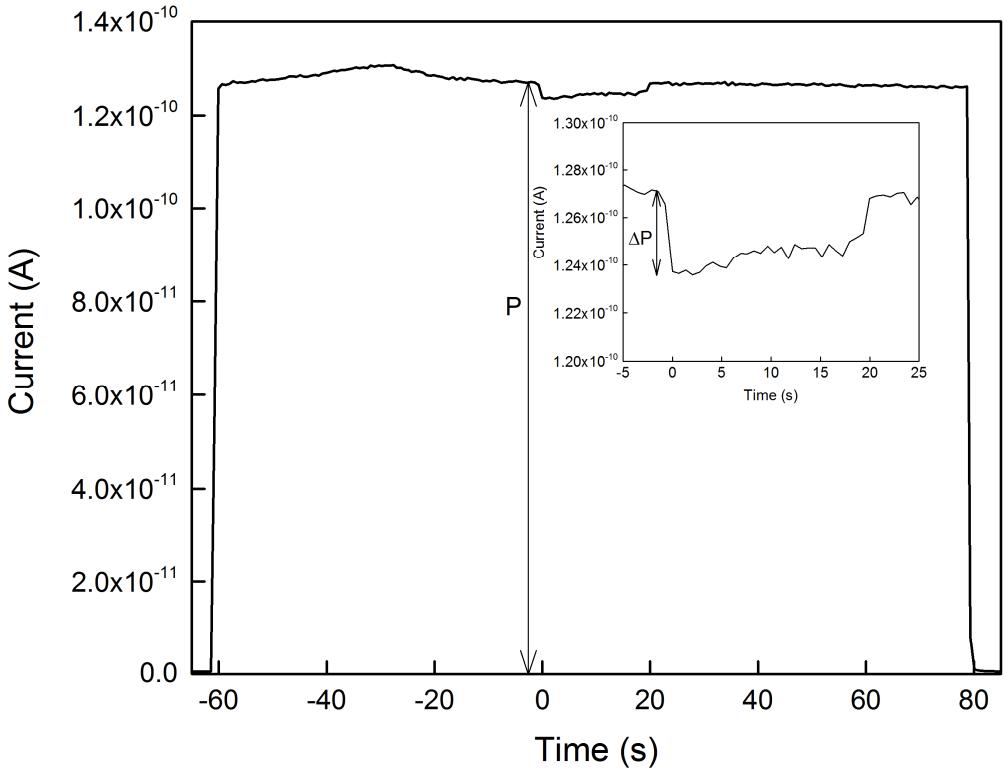


**Fig. S6.** King and Wells trace for the dissociative chemisorption of $CHD_3$ on Pt(111) at a surface temperature of 500 K and translational energy of 82 kJ/mol without laser excitation. The time axis has been shifted so that $t$ =0 s corresponds to the time when the inert beam flag was opened and the molecular beam hit the surface. The inset shows a magnification of the 20 s when the beam flag was open.

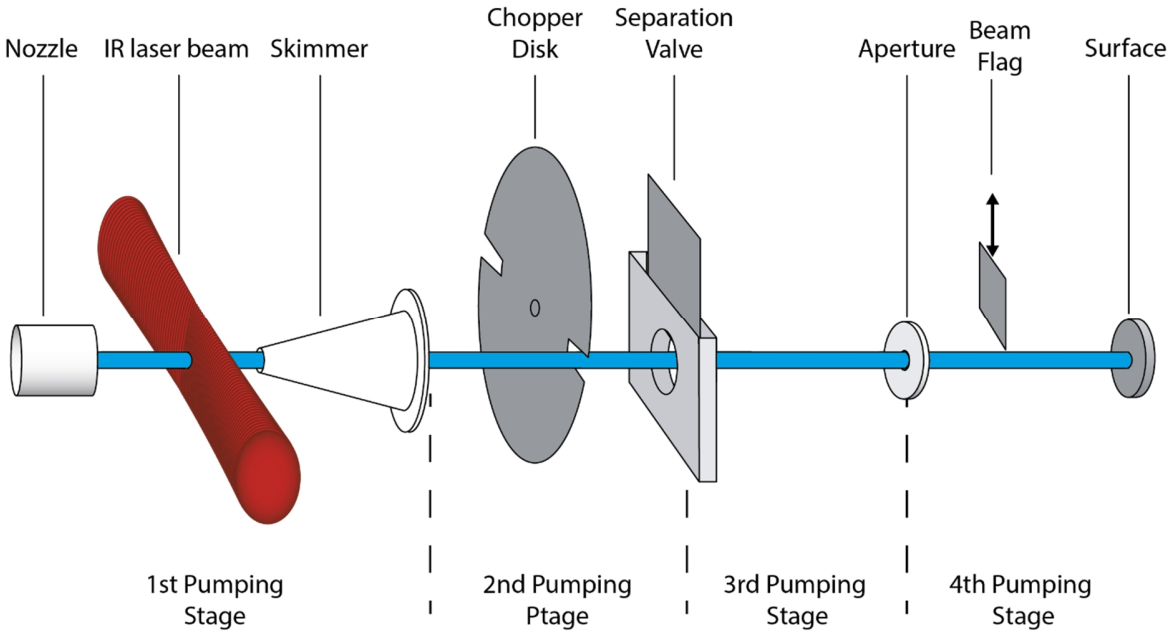


**Fig. S7**. A schematic overview of the molecular beam path used for the King and Wells measurements.

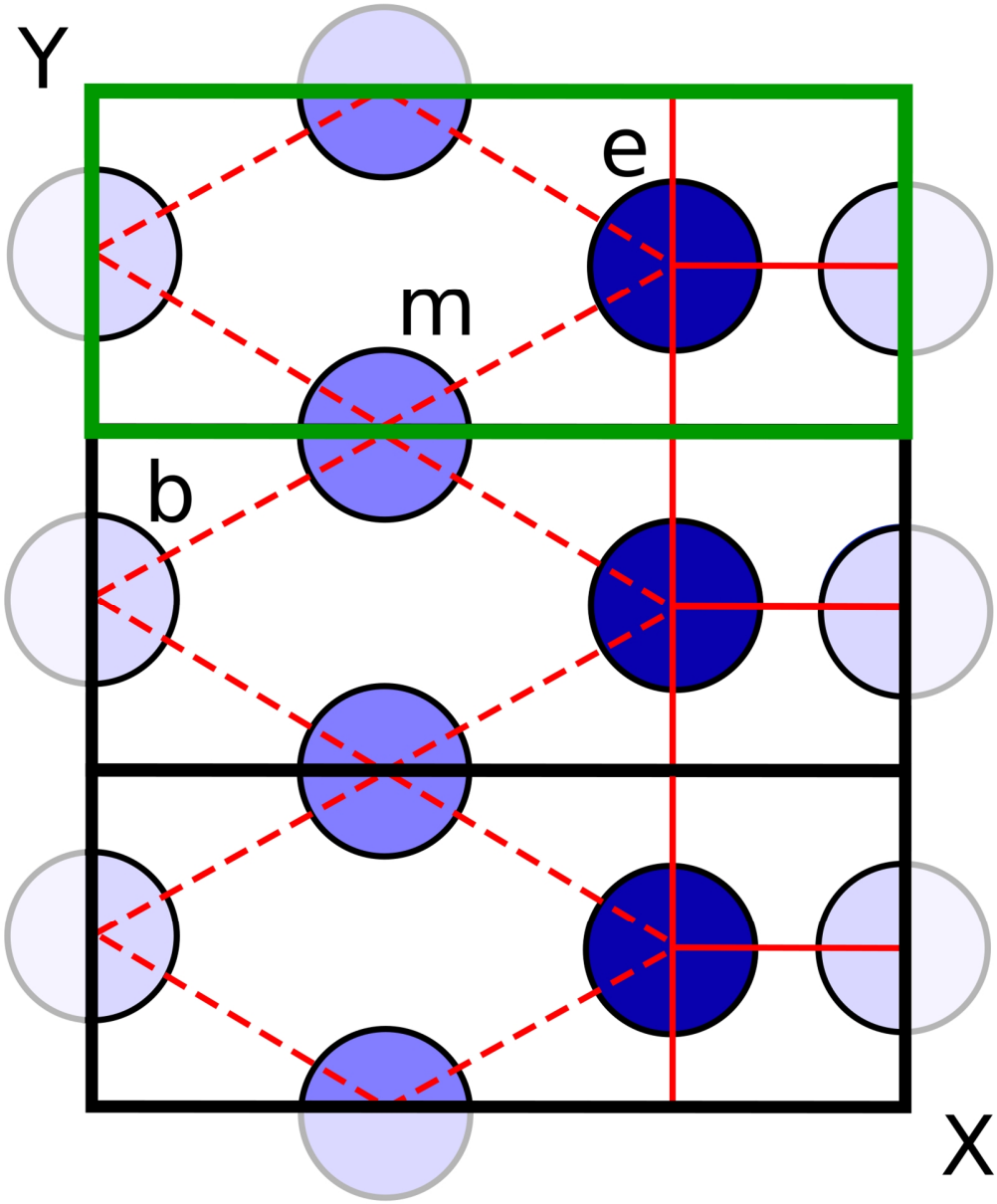


**Fig. S8.** Top view of the supercell used to simulate the Pt(211) slab. The 1x3 cell contains 3 times the irreducible unit cell (highlighted in green). The left part of the irreducible unit cell is characterized by the hexagonal (111) surface-like structure (red dashed lines) and the right part by the square (100) step (red full lines). The atoms are reported in blue and the color intensity is proportional to the height in Z. The letters mark the non-equivalent top sites investigated: edge (e), middle (m) and bottom (b).

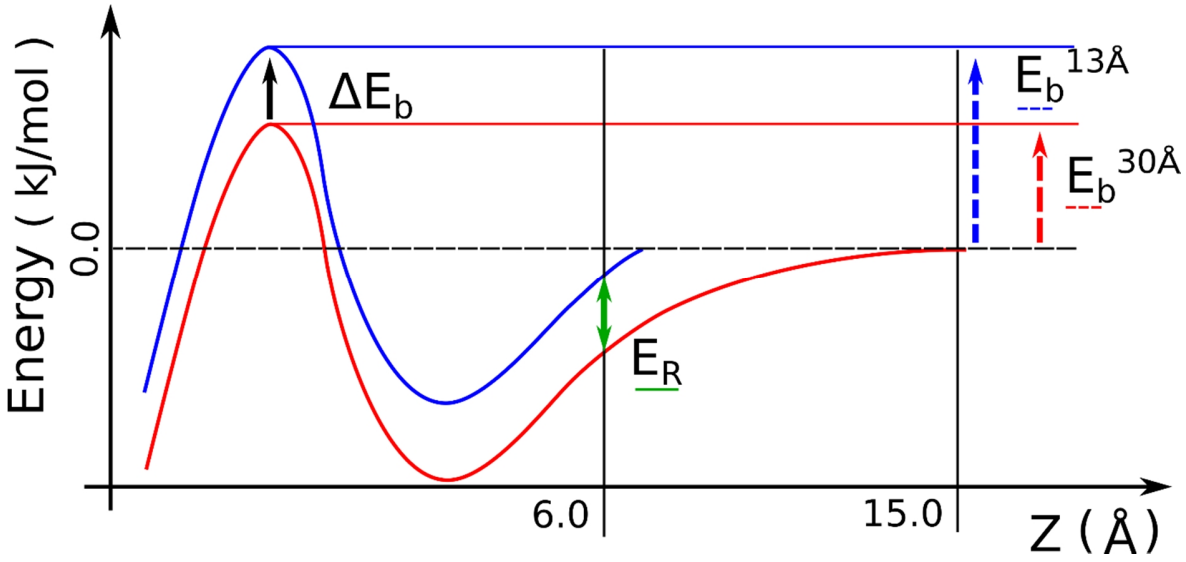


**Fig. S9.** Scheme of the barriers considered for $CH_4$ + Pt(111). The blue and the red curves refer to the 13 Å and to the 30 Å set up, respectively. The barrier heights $E_b^{13Å}$ and $E_b^{30Å}$ are shown as dashed arrows in the same color of the related curve. The residual energy $E_R$ is reported as a green arrow and the barrier height difference between the two vacuum sizes ($\Delta E_b$) is reported as a black arrow. Note that for the Pt(211) slab the gas phase, and therefore $E_R$, has been defined at 6.5 Å.

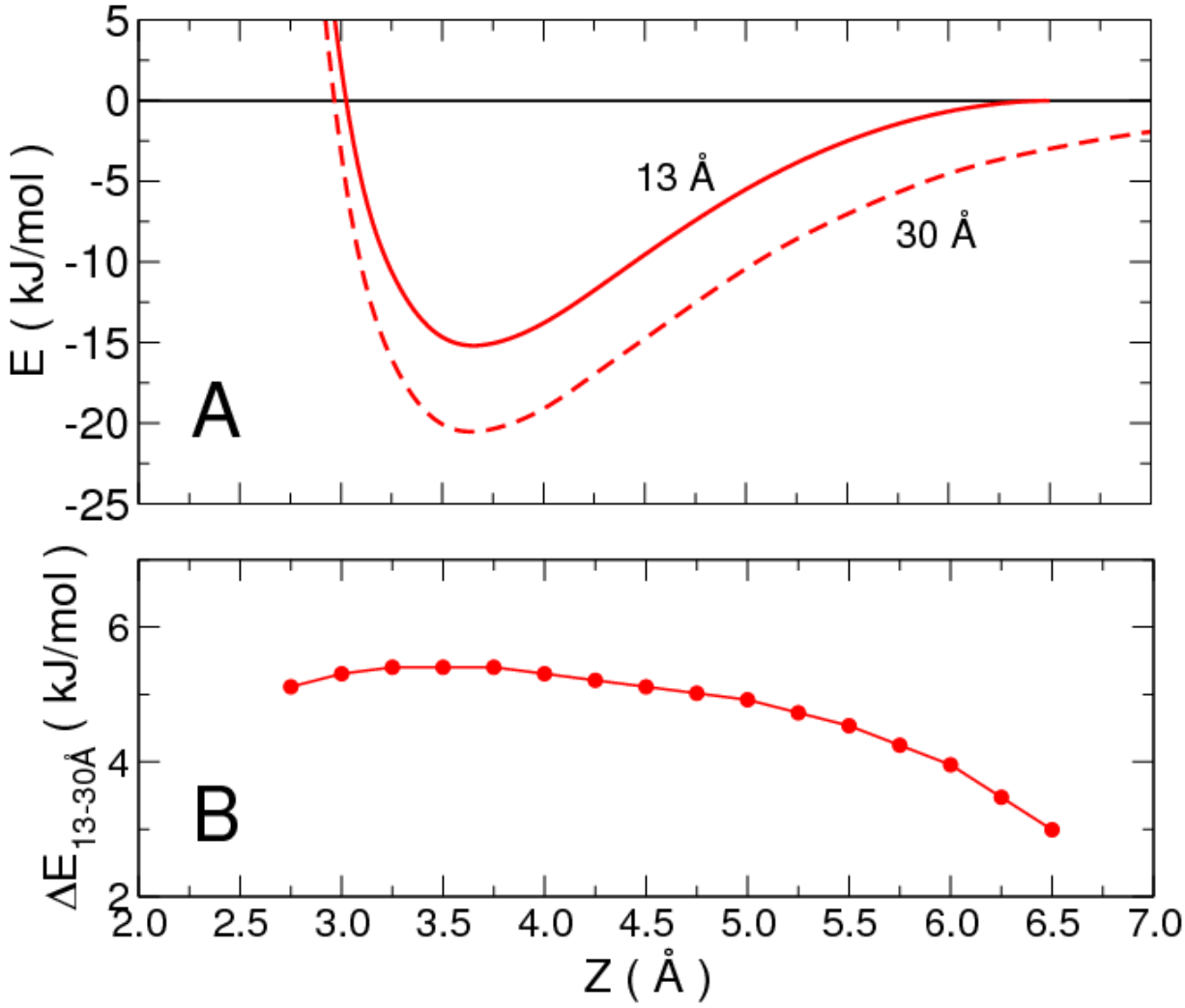


**Fig. S10.** Panel A: methane-surface interaction computed with 13 and 30 Å of vacuum (full and dashed red curves, respectively). Energies are reported with respect to the asymptotic energy. Panel B: difference between the 30 Å curve and the 13 Å curve (reported in panel A). Results for $CH_4$ + Pt(111).

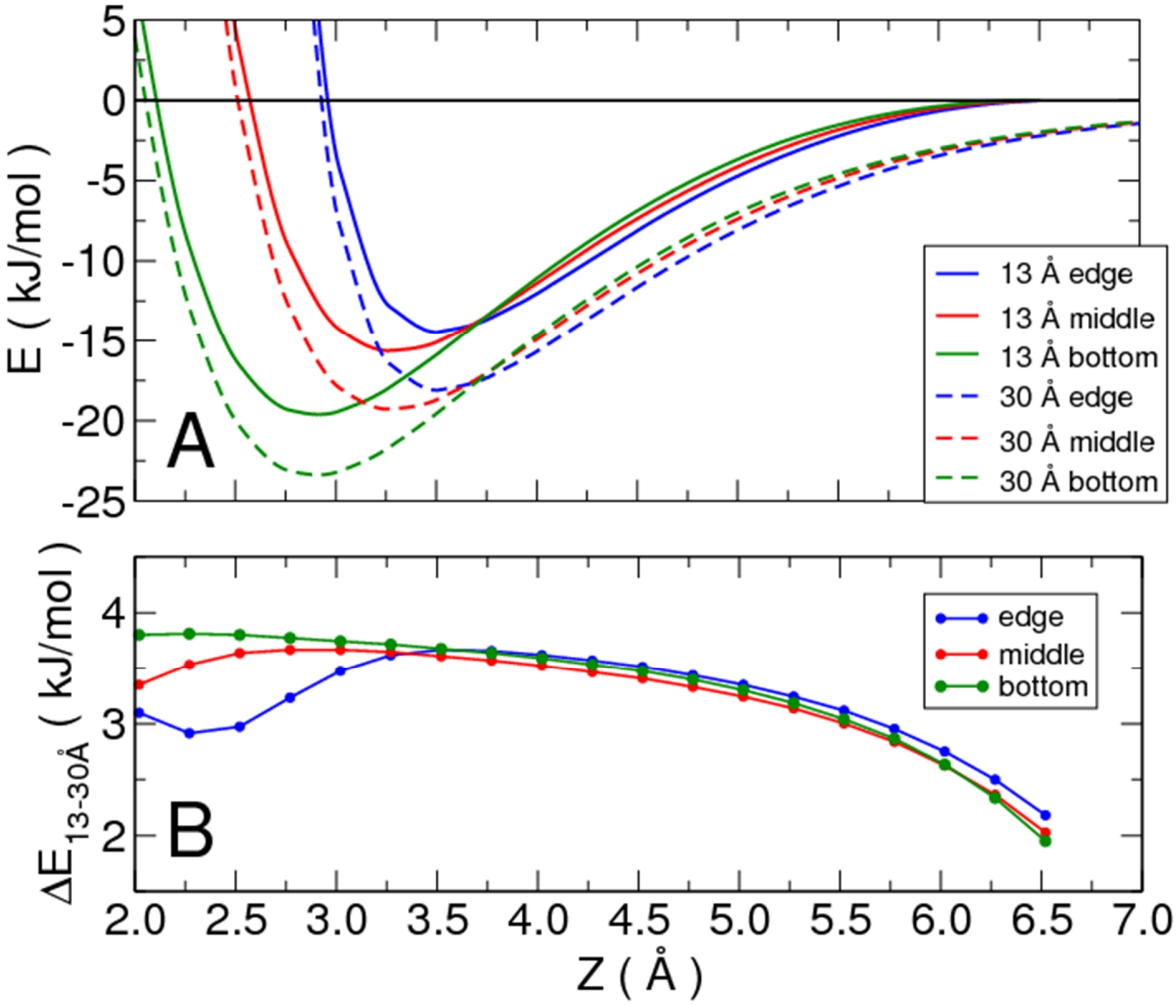


**Fig. S11.** Panel A: long range interactions computed with the 13 Å (solid lines) and 30 Å (dashed lines) vacuum distances. Panel B: difference between the two vacuum sizes. For both plots the colors represent the site above which the molecule is located (blue, red and green for edge, middle and bottom top respectively). Results for $CH_4$ + Pt(211).

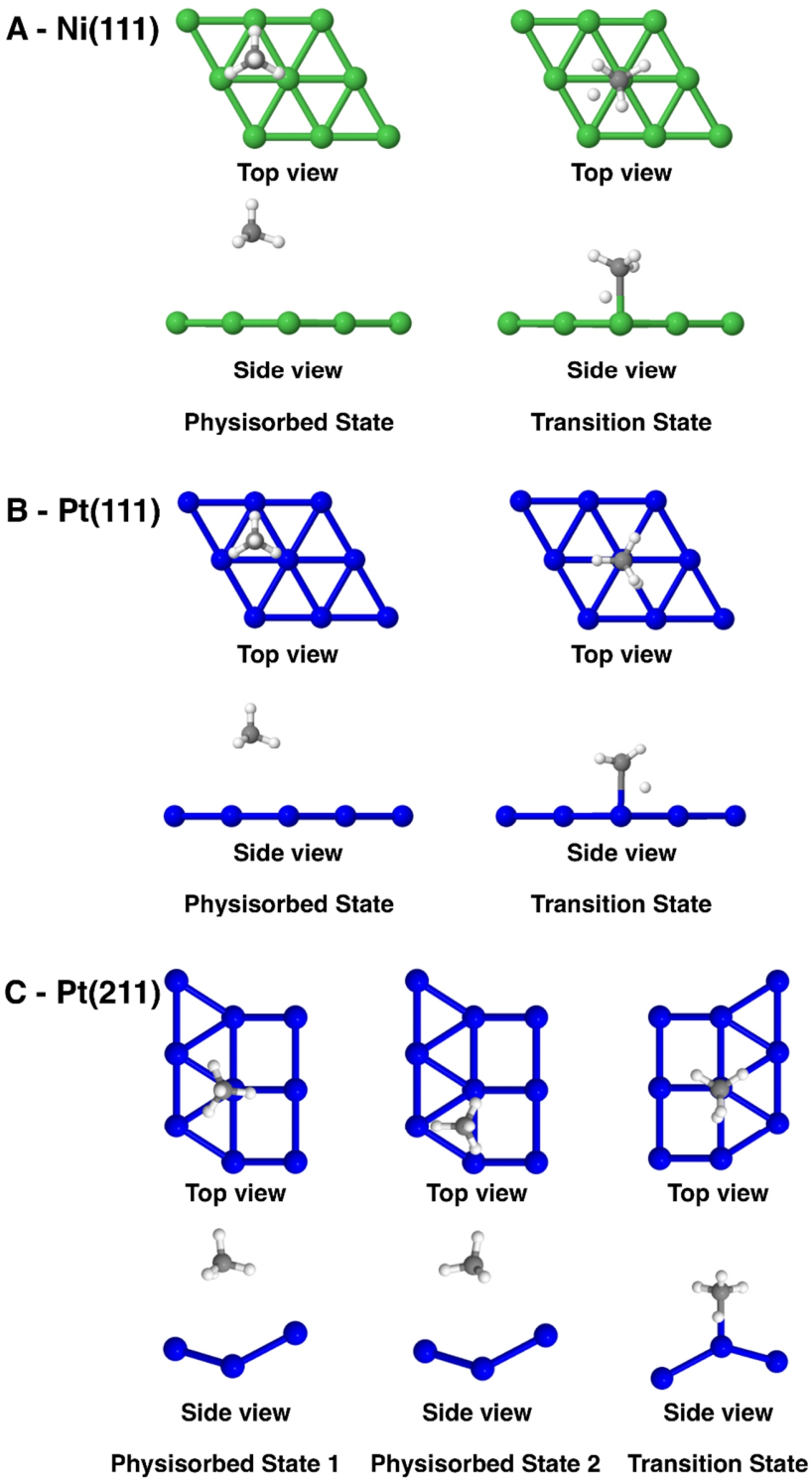


**Fig. S12.** Geometries of the TS with the minimum barrier height and of the molecular adsorption states in the vdW well for Ni(111), Pt(111) and Pt(211) (panels A, B and C, respectively).

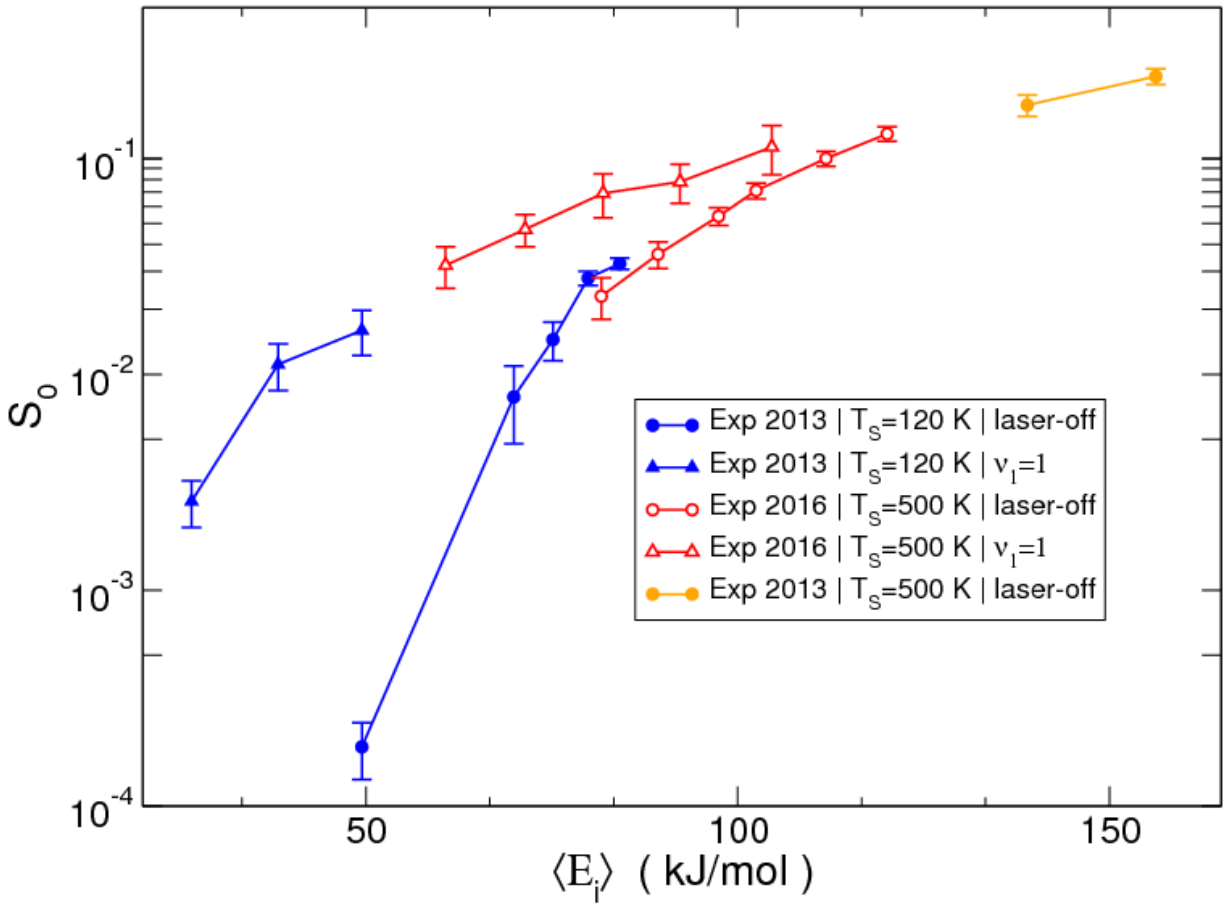


**Fig. S13** Available experimental zero coverage reaction probability ($S_0$) for the dissociation of $CHD_3$ on Pt(111) *vs*. the average beam kinetic energy ($\langle E_i \rangle$) for different surface temperatures. All the experimental data from 2013 and the AIMD results are taken from Ref.[5].

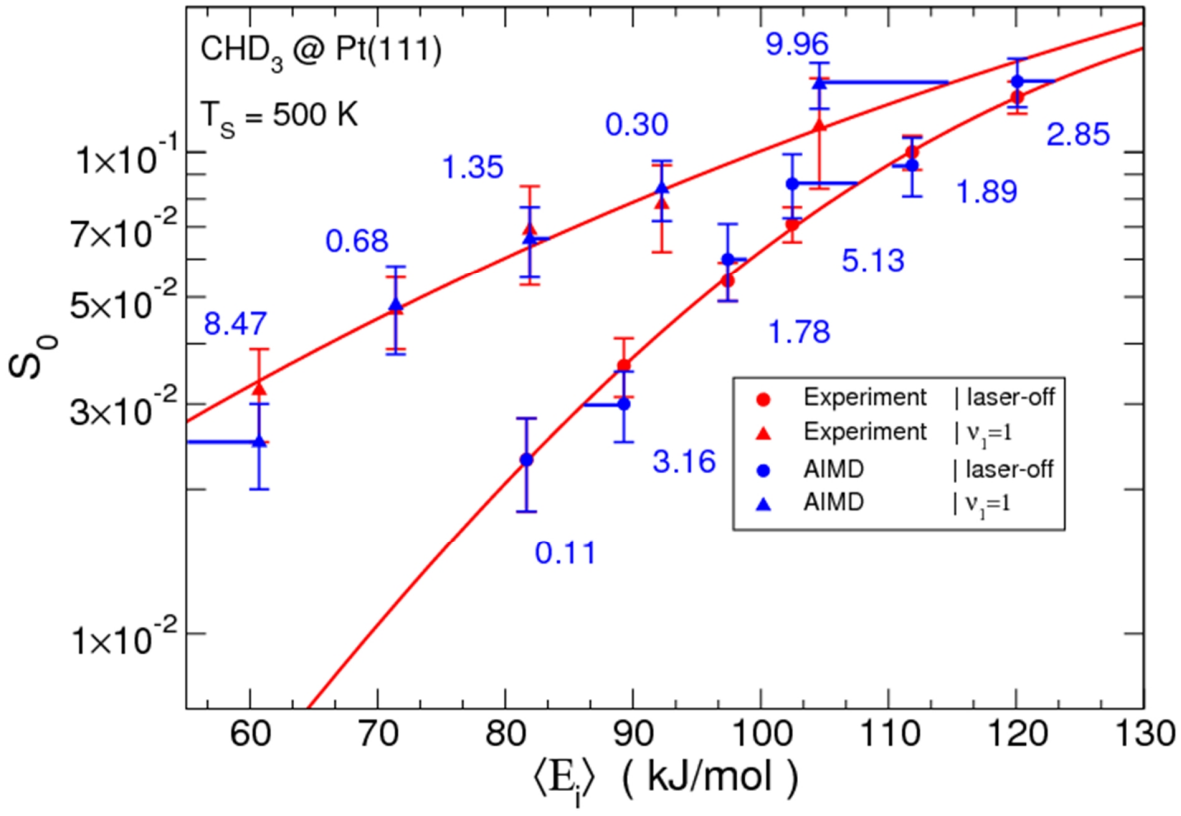


**Fig. S14.** Experimental and AIMD results (red and blue, respectively) for $CHD_3$ on Pt(111). The distances from the AIMD points to the fit (in kJ/mol) are reported in blue.

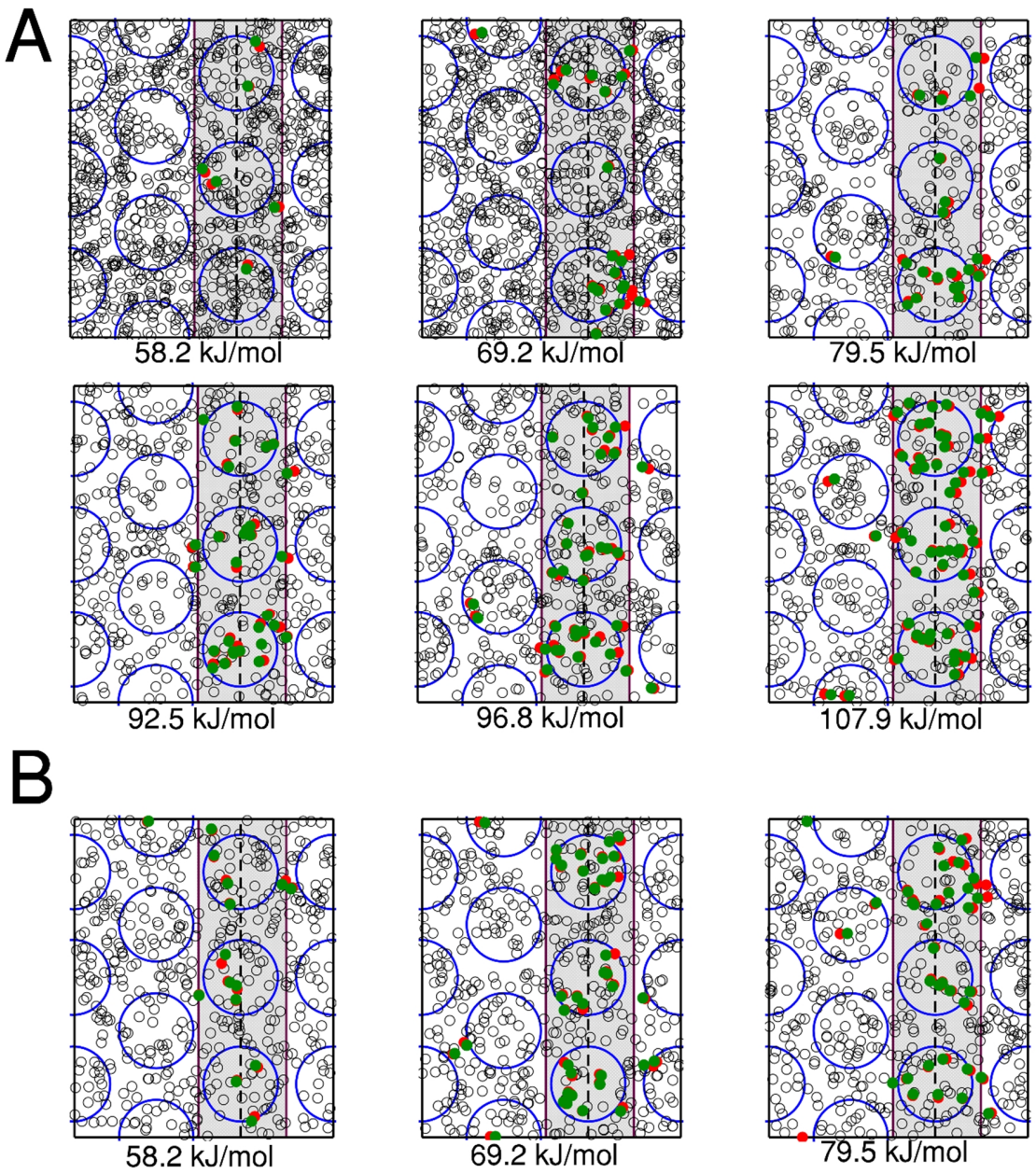


**Fig. S15.** Computed site reactivity on Pt(211). The figure shows the point of impact of molecules that react, at time 0 and at the time of reaction (see text for definition) in green and red respectively, and the initial positions of molecule that scatter in white. The step edge atoms are highlighted in gray. Panel A and B report results for laser-off and $\nu_1$=1 calculations, respectively.

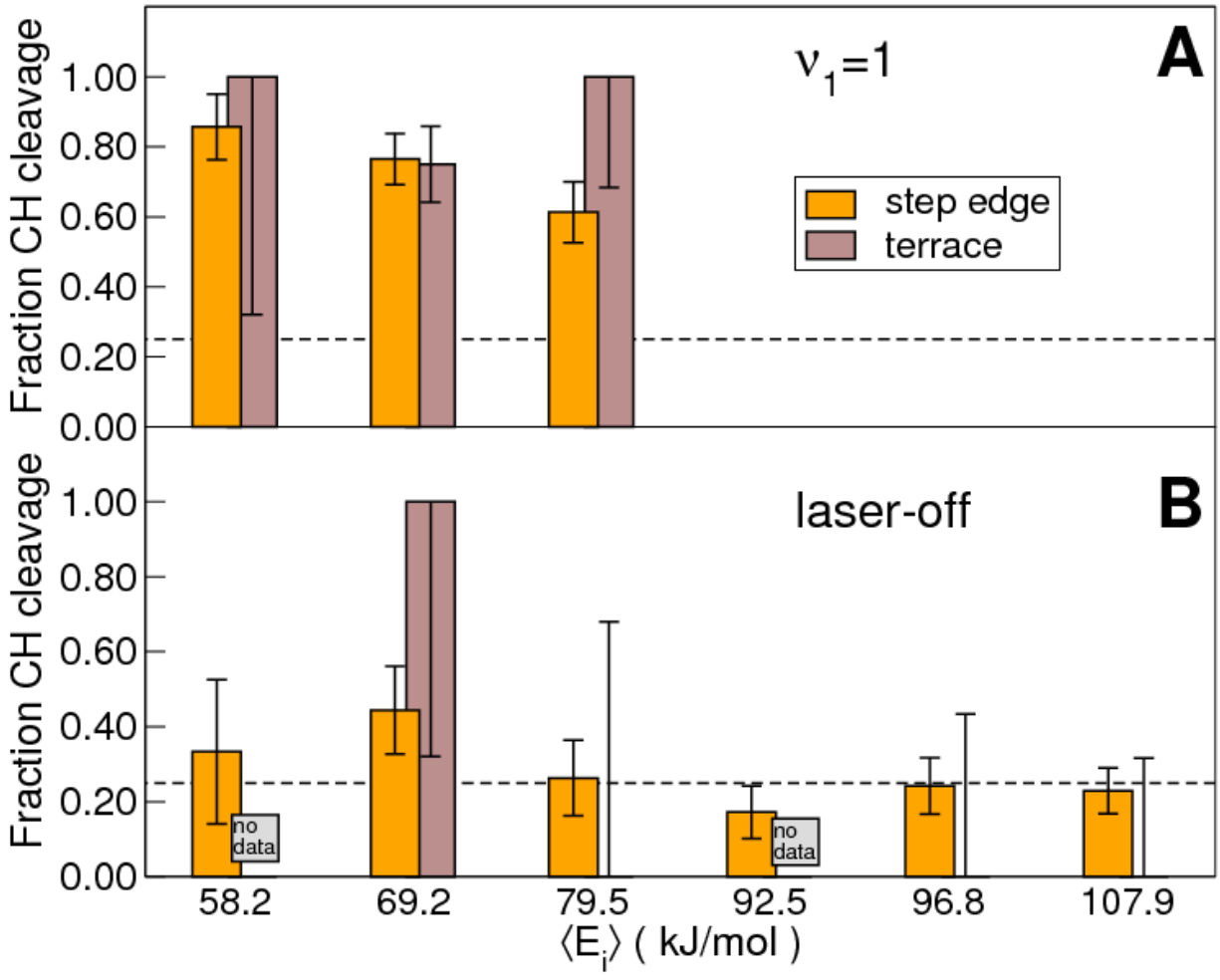


**Fig. S16.** Fraction of CH bond cleavage computed for $\nu_1$=1 (panel A) and laser-off (panel B) reaction. The results are reported in yellow and brown for step edge and terrace reactions respectively. For laser-off, no reaction occurred at the terrace for $\langle E_i \rangle$ = 58.2 and 92.5 kJ/mol.

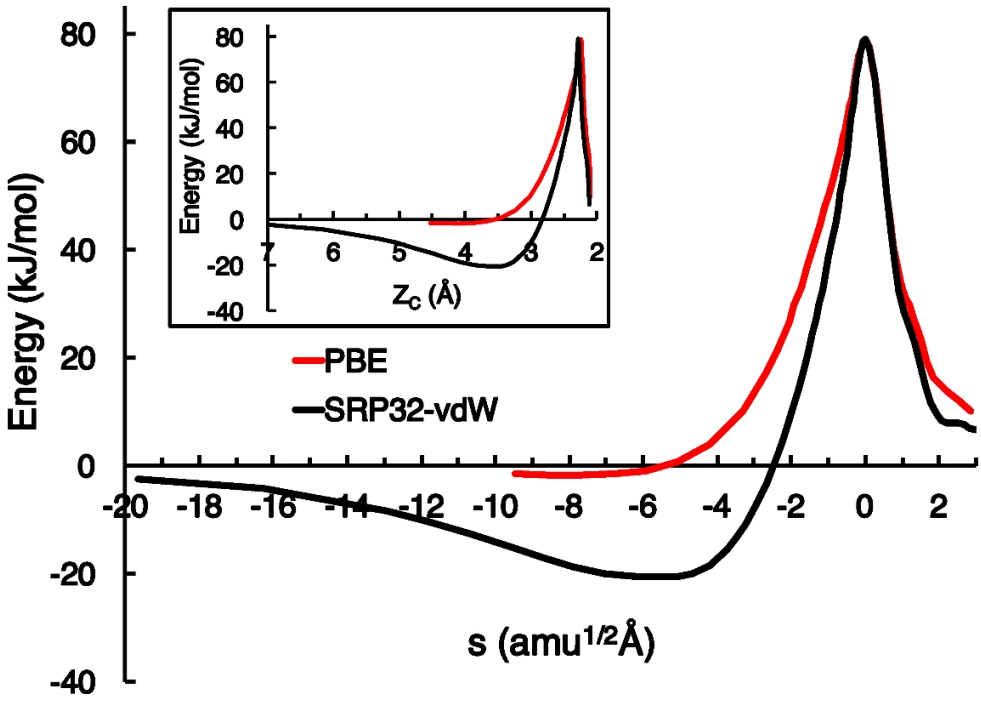


**Fig. S17.** The total energy, $V_0$, along the minimum energy path for methane dissociation on Pt(111), using both the PBE and SRP32-vdW functionals. $V_0$ is plotted as a function of both the path length, s, and in the inset, the distance of the carbon atom above the surface plane, $Z_C$.

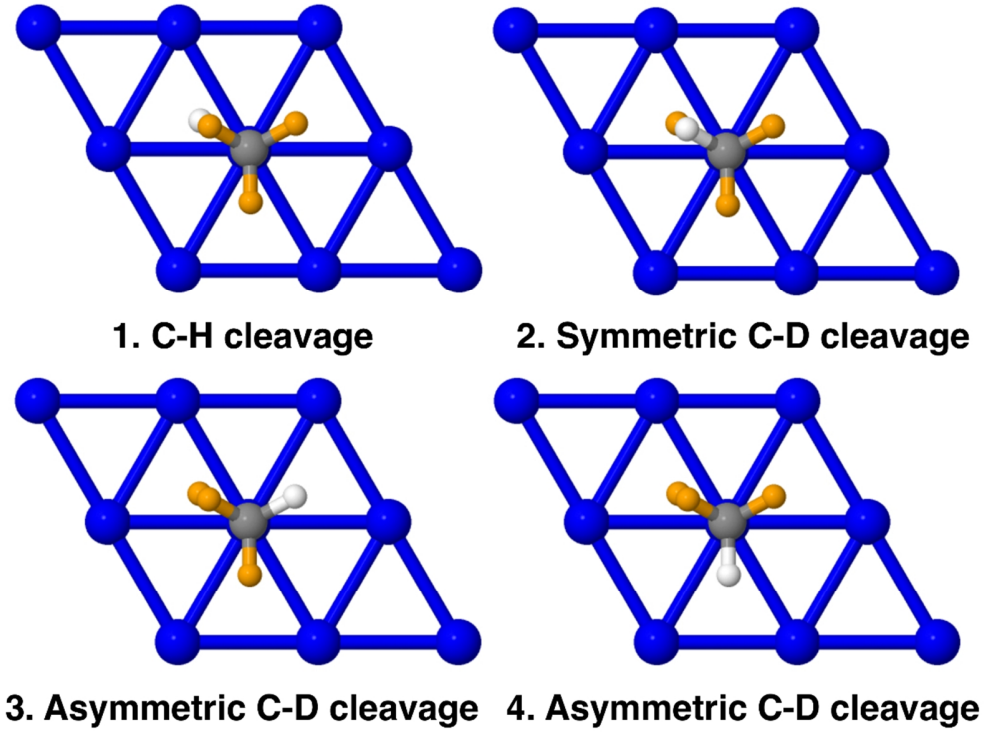


**Fig. S18.** The four unique transition state orientations for $CHD_3$ on Pt(111). The H atom is white.

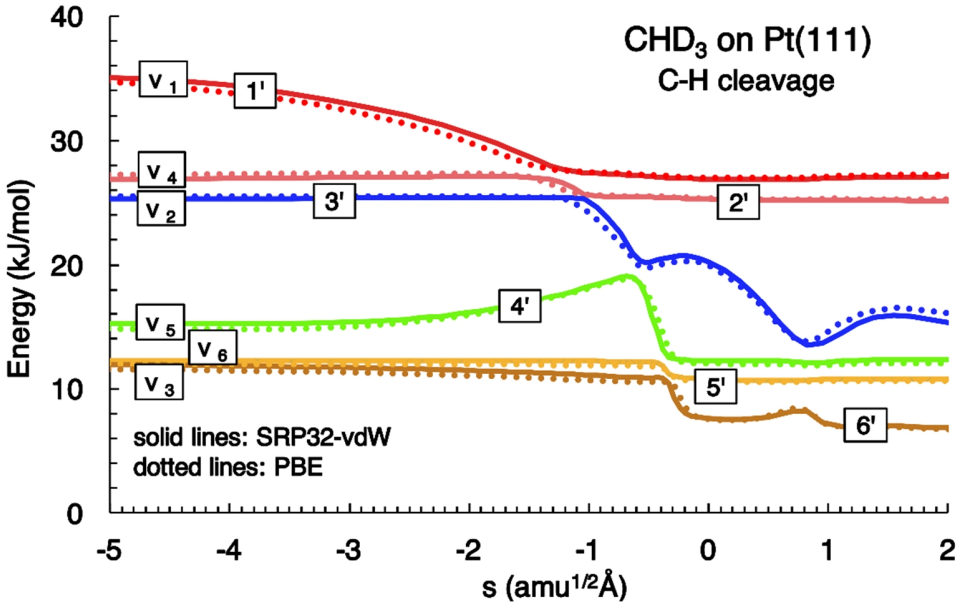


**Fig. S19.** Energies of the normal modes, $\hbar\omega_q(s)$, along the reaction path for the CH cleavage configuration of $CHD_3$ on Pt(111), using both the SRP and PBE functionals.

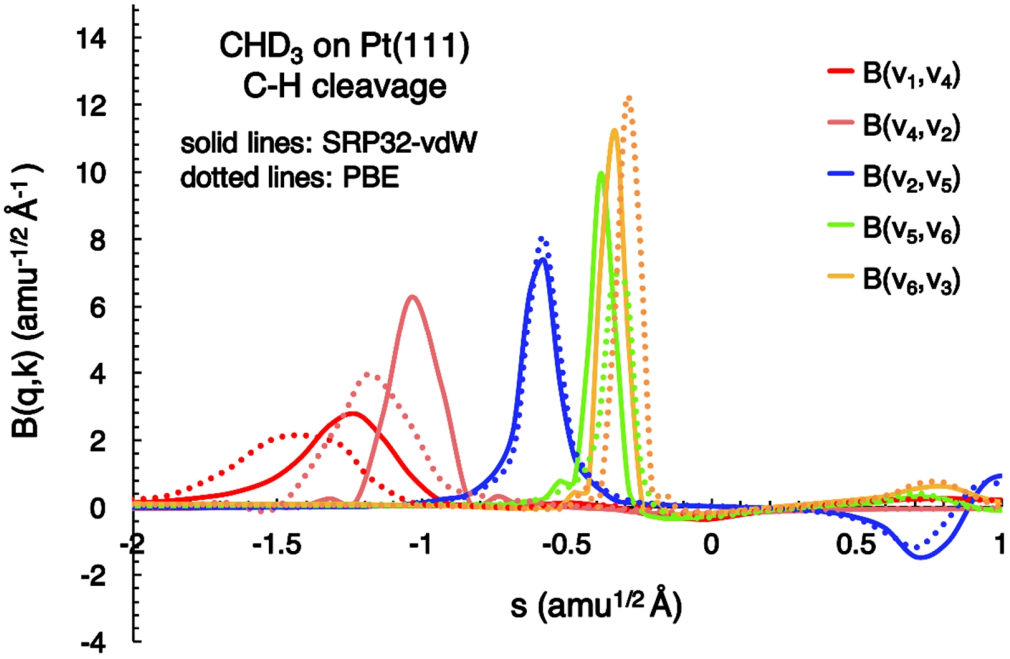


**Fig. S20.** Vibrationally nonadiabatic couplings, $B_{q,k}(s)$, along the reaction path for the dissociative chemisorption of $CHD_3$ on Pt(111), for the CH cleavage configuration.

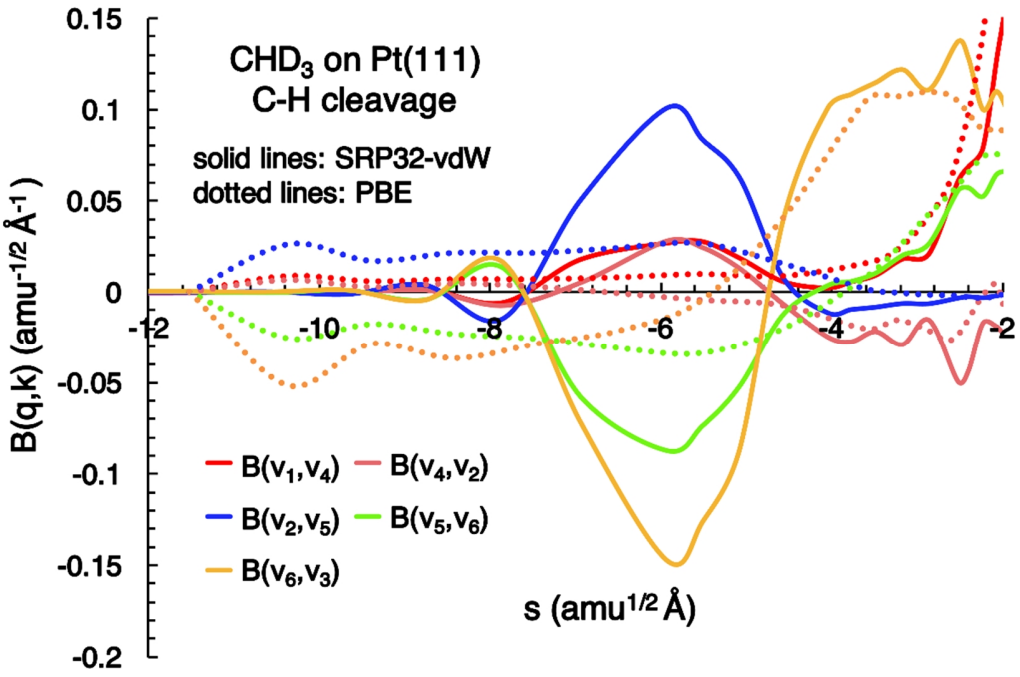


**Fig. S21.** Vibrationally nonadiabatic couplings, $B_{q,k}(s)$, along the reaction path in the entrance channel, for the CH cleavage configuration. Note the expanded scale from Fig. S20.

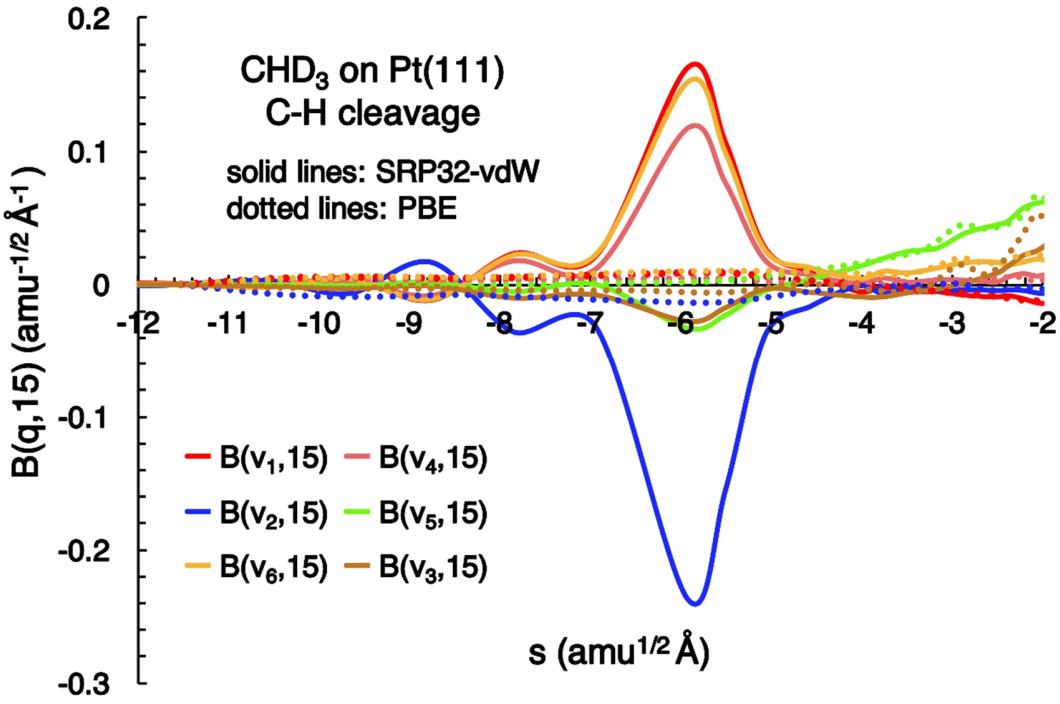


**Fig. S22.** Curvature couplings, $B_{q,15}(s)$, along the reaction path in the entrance channel, for the CH cleavage configuration.

**References**


(1) McCabe, P. R.; Juurlink, L. B. F.; Utz, A. L. A Molecular Beam Apparatus for Eigenstate-Resolved Studies of Gas-Surface Reactivity. *Rev. Sci. Instrum.* **2000**, *71*, 42–53.

(2) Chadwick, H.; Beck, R. D. Quantum State Resolved Gas-Surface Reaction Dynamics Experiments: A Tutorial Review. *Chem. Soc. Rev.* **2016**, *45*, 3576–3594.

(3) Chadwick, H.; Gutiérrez-González, A.; Beck, R. D. Quantum State Resolved Molecular Beam Reflectivity Measurements: $CH_4$ Dissociation on Pt(111). *J. Chem. Phys.* **2016**, *145*, 174707.

(4) Chen, L.; Ueta, H.; Chadwick, H.; Beck, R. D. The Negligible Role of C–H Stretch Excitation in the Physisorption of $CH_4$ on Pt(111). *J. Phys. Chem. C* **2015**, *119*, 14499–14505.

(5) Nattino, F.; Ueta, H.; Chadwick, H.; Reijzen, M. E. Van; Beck, R. D.; Jackson, B.; Hemert, M. C. Van; Kroes, G. J.; van Reijzen, M. E.; Beck, R. D.; et al. Ab Initio Molecular Dynamics Calculations versus Quantum-State-Resolved Experiments on $CHD_3$ + Pt(111): New Insights into a Prototypical Gas–Surface Reaction. *J. Phys. Chem. Lett.* **2014**, *5*, 1294–1299.

(6) Chen, L.; Ueta, H.; Bisson, R.; Beck, R. D. Vibrationally Bond-Selected Chemisorption of Methane Isotopologues on Pt(111) Studied by Reflection Absorption Infrared Spectroscopy. *Faraday Discuss.* **2012**, *157*, 285-295.

(7) Chen, L.; Ueta, H.; Bisson, R.; Beck, R. D. Quantum State-Resolved Gas/Surface Reaction Dynamics Probed by Reflection Absorption Infrared Spectroscopy. *Rev. Sci. Instrum.* **2013**, *84*, 53902.

(8) Ueta, H.; Chen, L.; Beck, R. D.; Colon-Diaz, I.; Jackson, B. Quantum State-Resolved $CH_4$

Dissociation on Pt(111): Coverage Dependent Barrier Heights from Experiment and Density Functional Theory. *Phys. Chem. Chem. Phys.* **2013**, *15*, 20526–20535.

(9) Hundt, P. M.; Ueta, H.; van Reijzen, M. E.; Jiang, B.; Guo, H.; Beck, R. D. Bond-Selective and Mode-Specific Dissociation of $CH_3D$ and $CH_2D_2$ on Pt(111). *J. Phys. Chem. A* **2015**, *119*, 12442–12448.

(10) Hundt, P. M.; van Reijzen, M. E.; Ueta, H.; Beck, R. D. Vibrational Activation of Methane Chemisorption: The Role of Symmetry. *J. Phys. Chem. Lett.* **2014**, *5*, 1963–1967.

(11) Nattino, F.; Migliorini, D.; Kroes, G. J.; Dombrowski, E.; High, E. A.; Killelea, D. R.; Utz, A. L. Chemically Accurate Simulation of a Polyatomic Molecule-Metal Surface Reaction. *J. Phys. Chem. Lett.* **2016**, *7*, 2402–2406.

(12) King, D. A.; Wells, M. G. Molecular Beam Investigation of Adsorption Kinetics on Bulk Metal Targets: Nitrogen on Tungsten. *Surf. Sci.* **1972**, *29*, 454–482.

(13) Chadwick, H.; Hundt, P. M.; van Reijzen, M. E.; Yoder, B. L.; Beck, R. D. Quantum State Specific Reactant Preparation in a Molecular Beam by Rapid Adiabatic Passage. *J. Chem. Phys.* **2014**, *140*, 34321.

(14) Yates, J. T. *Experimental Innovations in Surface Science: A Guide to Practical Laboratory Methods and Instruments*; Springer: New York, 1998.

(15) Scoles, G. *Atomic and Molecular Beam Methods*; Oxford University Press: New York, 1988.

(16) Yoder, B. L.; Bisson, R.; Hundt, P. M.; Beck, R. D. Alignment Dependent Chemisorption of Vibrationally Excited $CH_4(\nu_3)$ on Ni(100), Ni(110), and Ni(111). *J. Chem. Phys.* **2011**, *135* (22), 224703.

(17) Saëki, S.; Mizuno, M.; Kondo, S. Infrared Absorption Intensities of Methane and

Fluoromethanes. *Spectrochim. Acta Part A Mol. Spectrosc.* **1976**, *32*, 403–413.

(18) Hippler, M.; Quack, M. High-Resolution Fourier Transform Infrared and Cw-Diode Laser Cavity Ringdown Spectroscopy of the $\nu_2+2\nu_3$ Band of Methane near 7510 $cm^{-1}$ in Slit Jet Expansions and at Room Temperature. *J. Chem. Phys.* **2002**, *116*, 6045–6055.

(19) Juurlink, L. B. F.; McCabe, P. R.; Smith, R. R.; DiCologero, C. L.; Utz, A. L. Eigenstate-Resolved Studies of Gas-Surface Reactivity: $CH_4(\nu_3)$ Dissociation on Ni(100). *Phys. Rev. Lett.* **1999**, *83*, 868–871.

(20) Juurlink, L. B. F.; Killelea, D. R.; Utz, A. L. State-Resolved Probes of Methane Dissociation Dynamics. *Prog. Surf. Sci.* **2009**, *84*, 69–134.

(21) Fairbrother, D. H.; Peng, X. D.; Viswanathan, R.; Stair, P. C.; Trenary, M.; Fan, J. Carbon-Carbon Coupling of Methyl Groups on Pt(111). *Surf. Sci.* **1993**, *285*, L455–L460.

(22) Fairbrother, D. H.; Peng, X. D.; Trenary, M.; Stair, P. C. Surface Chemistry of Methyl Groups Adsorbed on Pt(111). *J. Chem. Soc. Faraday Trans.* **1995**, *91*, 3619–3625.

(23) Papp, C.; Fuhrmann, T.; Tränkenschuh, B.; Denecke, R.; Steinrück, H.-P. Kinetic Isotope Effects and Reaction Intermediates in the Decomposition of Methyl on Flat and Stepped Platinum (111) Surfaces. *Chem. Phys. Lett.* **2007**, *442*, 176–181.

(24) Badan, C.; Koper, M. T. M.; Juurlink, L. B. F. How Well Does Pt(211) Represent Pt[ n (111) × (100)] Surfaces in Adsorption/Desorption? *J. Phys. Chem. C* **2015**, *119*, 13551–13560.

(25) Campbell, C. T.; Ertl, G.; Kuipers, H.; Segner, J. A Molecular Beam Investigation of the Interactions of CO with a Pt(111) Surface. *Surf. Sci.* **1981**, *107*, 207–219.

(26) Jiang, L. Q.; Koel, B. E.; Falconer, J. L. Effects of K, O, and H Adatoms on the Adsorption Kinetics of CO on Pt(111). *Surf. Sci.* **1992**, *27*, 273–284.

(27) Creighan, S. C.; Mukerji, R. J.; Bolina, A. S.; Lewis, D. W.; Brown, W. A. The Adsorption of CO on the Stepped Pt{211} Surface: A Comparison of Theory and Experiment. *Catal. Letters* **2003**, *88*, 39–45.

(28) Mukerji, R. J.; Bolina, A. S.; Brown, W. A. A RAIRS and TPD Investigation of the Adsorption of CO on Pt{2 1 1}. *Surf. Sci.* **2003**, *527*, 198–208.

(29) Deng, R.; Herceg, E.; Trenary, M. Characterization of Methylidyne on Pt(1 1 1) with Infrared Spectroscopy. *Surf. Sci.* **2004**, *573*, 310–319.

(30) Smith, R. R.; Killelea, D. R.; Del Sesto, D. F.; Utz, A. L. Preference for Vibrational over Translational Energy in a Gas-Surface Reaction. *Science* **2004**, *304*, 992–995.

(31) Chuang, Y.-Y.; Radhakrishnan, M. L.; Fast, P. L.; Cramer, C. J.; Truhlar, D. G. Direct Dynamics for Free Radical Kinetics in Solution: Solvent Effect on the Rate Constant for the Reaction of Methanol with Atomic Hydrogen. *J. Phys. Chem. A* **1999**, *103*, 4893–4909.

(32) Diaz, C.; Pijper, E.; Olsen, R. A.; Busnengo, H. F.; Auerbach, D. J.; Kroes, G. J. Chemically Accurate Simulation of a Prototypical Surface Reaction: $H_2$ Dissociation on Cu(111). *Science* **2009**, *326*, 832–834.

(33) Sementa, L.; Wijzenbroek, M.; van Kolck, B. J.; Somers, M. F.; Al-Halabi, A.; Busnengo, H. F.; Olsen, R. A.; Kroes, G. J.; Rutkowski, M.; Thewes, C.; et al. Reactive Scattering of $H_2$ from Cu(100): Comparison of Dynamics Calculations Based on the Specific Reaction Parameter Approach to Density Functional Theory with Experiment. *J. Chem. Phys.* **2013**, *138*, 44708.

(34) Nour Ghassemi, E.; Wijzenbroek, M.; Somers, M. F.; Kroes, G. J. Chemically Accurate Simulation of Dissociative Chemisorption of $D_2$ on Pt(111). *Chem. Phys. Lett.* **2017**, *683*, 329-335.

(35) Dion, M.; Rydberg, H.; Schröder, E.; Langreth, D. C.; Lundqvist, B. I. Van Der Waals Density Functional for General Geometries. *Phys. Rev. Lett.* **2004**, *92*, 246401.

(36) Lee, K.; Murray, É. D.; Kong, L.; Lundqvist, B. I.; Langreth, D. C. Higher-Accuracy van Der Waals Density Functional. *Phys. Rev. B* **2010**, *82*, 081101.

(37) Groß, A.; Dianat, A. Hydrogen Dissociation Dynamics on Precovered Pd Surfaces: Langmuir Is Still Right. *Phys. Rev. Lett.* **2007**, *98*, 206107.

(38) Jiang, B.; Liu, R.; Li, J.; Xie, D.; Yang, M.; Guo, H. Mode Selectivity in Methane Dissociative Chemisorption on Ni(111). *Chem. Sci.* **2013**, *4*, 3249-3254.

(39) Shen, X.; Chen, J.; Zhang, Z.; Shao, K.; Zhang, D. H. Methane Dissociation on Ni(111): A Fifteen-Dimensional Potential Energy Surface Using Neural Network Method. *J. Chem. Phys.* **2015**, *143*, 144701.

(40) Hundt, P. M.; Jiang, B.; van Reijzen, M. E.; Guo, H.; Beck, R. D. Vibrationally Promoted Dissociation of Water on Ni(111). *Science* **2014**, *344*, 504–507.

(41) Nave, S.; Jackson, B. Vibrational Mode-Selective Chemistry: Methane Dissociation on Ni(100). *Phys. Rev. B - Condens. Matter Mater. Phys.* **2010**, *81*, 233408.

(42) Jackson, B.; Nave, S. The Dissociative Chemisorption of Methane on Ni(111): The Effects of Molecular Vibration and Lattice Motion. *J. Chem. Phys.* **2013**, *138*, 174705.

(43) Guo, H.; Jackson, B. Mode- and Bond-Selective Chemistry on Metal Surfaces: The Dissociative Chemisorption of $CHD_3$ on Ni(111). *J. Phys. Chem. C* **2015**, *119*, 14769–14779.

(44) Farjamnia, A.; Jackson, B. The Dissociative Chemisorption of Water on Ni(111): Mode- and Bond-Selective Chemistry on Metal Surfaces. *J. Chem. Phys.* **2015**, *142*, 234705.

(45) Nave, S.; Jackson, B. Methane Dissociation on Ni(111): The Role of Lattice Reconstruction.

*Phys. Rev. Lett.* **2007**, *98*, 173003.

(46) Luo, X.; Jiang, B.; Juaristi, J. I.; Alducin, M.; Guo, H. Electron-Hole Pair Effects in Methane Dissociative Chemisorption on Ni(111). *J. Chem. Phys.* **2016**, *145*, 44704.

(47) Blanco-Rey, M.; Juaristi, J. I.; Díez Muiño, R.; Busnengo, H. F.; Kroes, G. J.; Alducin, M. Electronic Friction Dominates Hydrogen Hot-Atom Relaxation on Pd(100). *Phys. Rev. Lett.* **2014**, *112*, 103203.

(48) Shakouri, K.; Behler, J.; Meyer, J.; Kroes, G. J. Accurate Neural Network Description of Surface Phonons in Reactive Gas–Surface Dynamics: $N_2$ + Ru(0001). *J. Phys. Chem. Lett.* **2017**, *8*, 2131–2136.

(49) Jackson, B.; Nave, S. The Dissociative Chemisorption of Methane on Ni(100): Reaction Path Description of Mode-Selective Chemistry. *J. Chem. Phys.* **2011**, *135*, 114701.

(50) Wang, X.-G.; Sibert, E. L. A Nine-Dimensional Perturbative Treatment of the Vibrations of Methane and its Isotopomers. *J. Chem. Phys.* **1999**, *111*, 4510–4522.

(51) Czakó, G.; Bowman, J. M. Dynamics of the Reaction of Methane with Chlorine Atom on an Accurate Potential Energy Surface. *Science* **2011**, *334*, 343–346.

(52) Kao, C.-L.; Madix, R. J. The Adsorption Dynamics of Small Alkanes on (111) Surfaces of Platinum Group Metals. *Surf. Sci.* **2004**, *557*, 215–230.

(53) Lyon, H. B.; Somorjai, G. A. Surface Debye Temperatures of the (100), (111), and (110) Faces of Platinum. *J. Chem. Phys.* **1966**, *44*, 3707–3711.

(54) Weinberg, W. H. Application of the Debye□Waller Theory to Atomic and Molecular Scattering from Solid Surfaces. *J. Chem. Phys.* **1972**, *57*, 5463–5466.

(55) Takeuchi, W.; Yamamura, Y. Ne Neutral Atoms 180° Backscattered from a Pt(111) Surface in the Three-Atom Scattering Model. *Surf. Sci.* **1992**, *277*, 351–358.

(56) Manson J. R. Energy Transfer to Phonons in Atom and Molecule Collisions with Surfaces in *Handbook of Surface Science, Vol* 3; Eds. Hasselbrink, E.; Lundqvist, B. I.; Elsevier Science: Oxford, U.K.; **2008**.

(57) Manson, J. R. Inelastic Scattering from Surfaces. *Phys. Rev. B* **1991**, *43*, 6924–6937.

(58) Manson, J. R. Multiphonon Atom-Surface Scattering. *Comput. Phys. Commun.* **1994**, *80*, 145–167.

(59) Chakraborty, A.; Zhao, Y.; Lin, H.; Truhlar, D. G. Combined Valence Bond-Molecular Mechanics Potential-Energy Surface and Direct Dynamics Study of Rate Constants and Kinetic Isotope Effects for the $H+C_2H_6$ Reaction. *J. Chem. Phys.* **2006**, *124*, 44315.

(60) Nattino, F.; Díaz, C.; Jackson, B.; Kroes, G. J. Effect of Surface Motion on the Rotational Quadrupole Alignment Parameter of $D_2$ on Cu(111). *Phys. Rev. Lett.* **2012**, *108*, 236104.

(61) Nieto, P.; Farías, D.; Miranda, R.; Luppi, M.; Baerends, E. J.; Somers, M. F.; van der Niet, M. J. T. C.; Olsen, R. A.; Kroes, G. J. Diffractive and Reactive Scattering of $H_2$ from Ru(0001): Experimental and Theoretical Study. *Phys. Chem. Chem. Phys.* **2011**, *13*, 8583.

(62) Groot, I. M. N.; Ueta, H.; van der Niet, M. J. T. C.; Kleyn, A. W.; Juurlink, L. B. F. Supersonic Molecular Beam Studies of Dissociative Adsorption of $H_2$ on Ru(0001). *J. Chem. Phys.* **2007**, *127*, 244701.

(63) Wijzenbroek, M.; Kroes, G. J. The Effect of the Exchange-Correlation Functional on $H_2$ Dissociation on Ru(0001). *J. Chem. Phys.* **2014**, *140*, 84702.

(64) Nattino, F.; Migliorini, D.; Bonfanti, M.; Kroes, G. J. Methane Dissociation on Pt(111): Searching for a Specific Reaction Parameter Density Functional. *J. Chem. Phys.* **2016**, *144*, 44702.

(65) Perdew, J. P.; Burke, K.; Ernzerhof, M. Generalized Gradient Approximation Made Simple.

*Phys. Rev. Lett.* **1996**, *77*, 3865–3868.

(66) Hammer, B.; Hansen, L. B.; Nørskov, J. K. Improved Adsorption Energetics within Density-Functional Theory Using Revised Perdew-Burke-Ernzerhof Functionals. *Phys. Rev. B* **1999**, *59*, 7413–7421.

(67) Román-Pérez, G.; Soler, J. M. Efficient Implementation of a van Der Waals Density Functional: Application to Double-Wall Carbon Nanotubes. *Phys. Rev. Lett.* **2009**, *103*, 096102.

(68) Wijzenbroek, M.; Klein, D. M.; Smits, B.; Somers, M. F.; Kroes, G. J. Performance of a Non-Local van Der Waals Density Functional on the Dissociation of $H_2$ on Metal Surfaces. *J. Phys. Chem. A* **2015**, *119*, 12146–12158.

(69) Berland, K.; Cooper, V. R.; Lee, K.; Schröder, E.; Thonhauser, T.; Hyldgaard, P.; Lundqvist, B. I. Van Der Waals Forces in Density Functional Theory: A Review of the vdW-DF Method. *Reports Prog. Phys.* **2015**, *78*, 066501.

(70) Perdew, J. P.; Ruzsinszky, A.; Tao, J.; Staroverov, V. N.; Scuseria, G. E.; Csonka, G. I. Prescription for the Design and Selection of Density Functional Approximations: More Constraint Satisfaction with Fewer Fits. *J. Chem. Phys.* **2005**, *123*, 62201.

(71) Thonhauser, T.; Zuluaga, S.; Arter, C. A.; Berland, K.; Schroöder, E.; Hyldgaard, P. Spin Signature of Nonlocal Correlation Binding in Metal-Organic Frameworks. *Phys. Rev. Lett.* **2015**, *115*, 136402.

(72) Giannozzi, P.; Baroni, S.; Bonini, N.; Calandra, M.; Car, R.; Cavazzoni, C.; Ceresoli, D.; Chiarotti, G. L.; Cococcioni, M.; Dabo, I.; et al. QUANTUM ESPRESSO: a Modular and Open-Source Software Project for Quantum Simulations of Materials. *J. Phys. Condens. Matt.* **2009**, *21*, 395502.

(73) Marques, M. A. L.; Oliveira, M. J. T.; Burnus, T. LIBXC: A Library of Exchange and Correlation Functionals for Density Functional Theory. *Comput. Phys. Commun.* **2012**, *183*, 2272–2281.

(74) Kresse, G.; Joubert, D. From Ultrasoft Pseudopotentials to the Projector Augmented-Wave Method. *Phys. Rev. B* **1999**, *59*, 1758–1775.

(75) Blöchl, P. E. Projector Augmented-Wave Method. *Phys. Rev. B* **1994**, *50*, 17953–17979.

(76) Dal Corso, A. Pseudopotentials Periodic Table: From H to Pu. *Comp. Mater. Sci.* **2014**, *95*, 337–350.

(77) Perdew, J. P.; Burke, K.; Ernzerhof, M. Erratum: Generalized Gradient Approximation Made Simple. *Phys. Rev. Lett.* **1997**, *78*, 1396-1396.

(78) Thonhauser, T.; Cooper, V. R.; Li, S.; Puzder, A.; Hyldgaard, P.; Langreth, D. C. Van Der Waals Density Functional: Self-Consistent Potential and the Nature of the van Der Waals Bond. *Phys. Rev. B* **2007**, *76*, 125112.

(79) Langreth, D. C.; Lundqvist, B. I.; Chakarova-Käck, S. D.; Cooper, V. R.; Dion, M.; Hyldgaard, P.; Kelkkanen, A.; Kleis, J.; Kong, L.; Li, S.; et al. A Density Functional for Sparse Matter. *J. Phys. Condens. Matt.* **2009**, *21*, 084203.

(80) Zhang, Y.; Yang, W. Comment on "Generalized Gradient Approximation Made Simple." *Phys. Rev. Lett.* **1998**, *80*, 890–890.

(81) Kresse, G.; Hafner, J. *Ab Initio* Molecular Dynamics for Liquid Metals. *Phys. Rev. B* **1993**, *47*, 558–561.

(82) Kresse, G.; Hafner, J. *Ab Initio* Molecular-Dynamics Simulation of the Liquid-Metal–Amorphous-Semiconductor Transition in Germanium. *Phys. Rev. B* **1994**, *49*, 14251–14269.

(83) Arblaster, J. W. Crystallographic Properties of Platinum. *Platin. Met. Rev*. **2006**, 50, 118–119.

(84) Arblaster, J. W. Crystallographic Properties of Platinum. *Platin. Met. Rev*. **1997**, *41*, 12–21.

(85) Xiao, P.; Sheppard, D.; Rogal, J.; Henkelman, G. Solid-State Dimer Method for Calculating Solid-Solid Phase Transitions. *J. Chem. Phys.* **2014**, *140*, 174104.

(86) Kästner, J.; Sherwood, P. Superlinearly Converging Dimer Method for Transition State Search. *J. Chem. Phys.* **2008**, *128*, 014106.

(87) Heyden, A.; Bell, A. T.; Keil, F. J. Efficient Methods for Finding Transition States in Chemical Reactions: Comparison of Improved Dimer Method and Partitioned Rational Function Optimization Method. *J. Chem. Phys*. **2005**, *123*, 224101.

(88) Henkelman, G.; Jónsson, H. A Dimer Method for Finding Saddle Points on High Dimensional Potential Surfaces Using Only First Derivatives. *J. Chem. Phys*. **1999**, *111*, 7010–7022.

(89) Tiwari, A. K.; Nave, S.; Jackson, B. Methane Dissociation on Ni(111): A New Understanding of the Lattice Effect. *Phys. Rev. Lett.* **2009**, *103*, 253201.

(90) Nave, S.; Tiwari, A. K.; Jackson, B. Methane Dissociation and Adsorption on Ni(111), Pt(111), Ni(100), Pt(100), and Pt(110)-(1×2): Energetic Study. *J. Chem. Phys.* **2010**, *132*, 054705.

(91) Orita, H.; Itoh, N.; Inada, Y. A Comparison of CO Adsorption on Pt(211), Ni(211), and Pd(211) Surfaces Using Density Functional Theory. *Surf. Sci.* **2004**, *571*, 161–172.

(92) Díaz, C.; Olsen, R. A.; Auerbach, D. J.; Kroes, G. J. Six-Dimensional Dynamics Study of Reactive and Non Reactive Scattering of $H_2$ from Cu(111) Using a Chemically Accurate Potential Energy Surface. *Phys. Chem. Chem. Phys.* **2010**, *12*, 6499-6519.

(93) Watanabe, K.; Matsumoto, Y. Comparative Study of Photochemistry of Methane on Pt(111) and Pd(111) Surfaces. *Surf. Sci.* **1997**, *390*, 250–255.

(94) Simpson, W. R.; Rakitzis, T. P.; Kandel, S. A.; Orr□Ewing, A. J.; Zare, R. N. Reaction of Cl with Vibrationally Excited $CH_4$ and $CHD_3$ : State□to□State Differential Cross Sections and Steric Effects for the HCl Product. *J. Chem. Phys.* **1995**, *103*, 7313–7335.

(95) Stouffer, S. A.; Suchman, E. A.; DeVinney, L. C.; Star, S. A.; Williams Jr, R. M. The American Soldier: Adjustment during Army life.(Studies in Social Psychology in World War II), Vol. 1. **1949**.

(96) Nattino, F.; Genova, A.; Guijt, M.; Muzas, A. S.; Díaz, C.; Auerbach, D. J.; Kroes, G. J. Dissociation and Recombination of $D_2$ on Cu(111): *Ab Initio* Molecular Dynamics Calculations and Improved Analysis of Desorption Experiments. *J. Chem. Phys.* **2014**, *141*, 124705.

(97) Frenkel, J. Theorie Der Adsorption Und Verwandter Erscheinungen. *Z. Phys.* **1924**, *26*, 117–138.

(98) Liang, Z.; Li, T.; Kim, M.; Asthagiri, A.; Weaver, J. F. Low-Temperature Activation of Methane on the $IrO_2$ (110) Surface. *Science* **2017**, *356*, 299–303.

(99) Dombrowski, E.; Peterson, E.; Del Sesto, D.; Utz, A. L. Precursor-Mediated Reactivity of Vibrationally Hot Molecules: Methane Activation on Ir(111). *Catal. Today* **2015**, *244*, 10–18.

(100) Szuromi, P. D.; Engstrom, J. R.; Weinberg, W. H. Adsorption and Reaction of N-Alkanes on the platinum(110)-(1 x 2) Surface. *J. Phys. Chem.* **1985**, *89*, 2497–2502.

(101) Wittrig, T. S.; Szuromi, P. D.; Weinberg, W. H. The Interaction of Ethane, Propane, Isobutane, and Neopentane with the (110) Surface of Iridium. *J. Chem. Phys.* **1982**, *76*,

3305–3315.

(102) Mullins, C. B.; Weinberg, W. H. Trapping□Mediated Dissociative Chemisorption of Ethane on Ir(110)□(1×2). *J. Chem. Phys.* **1990**, *92*, 4508–4512.

(103) Hamza, A. V.; Steinruck, H. □P.; Madix, R. J. The Dynamics of the Dissociative Adsorption of Alkanes on Ir(110). *J. Chem. Phys.* **1987**, *86*, 6506–6514.

(104) Gundersen, K.; Jacobsen, K. W.; Nørskov, J. K. The Energetics and Dynamics of $H_2$ Dissociation on Al(110). *Surf. Sci.* **1994**, *304*, 131–144.

(105) Polanyi, J. C. Some Concepts in Reaction Dynamics. *Science* **1987**, *236*, 680–690.

(106) Louis, T. A. Confidence Intervals for a Binomial Parameter after Observing No Successes. *Am. Stat.* **1981**, *35*, 154-154.

(107) Miller, W. H.; Handy, N. C.; Adams, J. E. Reaction Path Hamiltonian for Polyatomic Molecules. *J. Chem. Phys.* **1980**, *72*, 99–112.

(108) Han, D.; Nave, S.; Jackson, B. Dissociative Chemisorption of Methane on Pt(110)-(1×2): Effects of Lattice Motion on Reactions at Step Edges. *J. Phys. Chem. A* **2013**, *117*, 8651–8659.

(109) Jackson, B.; Nattino, F.; Kroes, G. J. Dissociative Chemisorption of Methane on Metal Surfaces: Tests of Dynamical Assumptions Using Quantum Models and Ab Initio Molecular Dynamics. *J. Chem. Phys.* **2014**, *141*, 054102.

(110) Nave, S.; Tiwari, A. K.; Jackson, B. Dissociative Chemisorption of Methane on Ni and Pt Surfaces: Mode-Specific Chemistry and the Effects of Lattice Motion. *J. Phys. Chem. A* **2014**, *118*, 9615–9631.

(111) Guo, H.; Jackson, B. Mode-Selective Chemistry on Metal Surfaces: The Dissociative Chemisorption of $CH_4$ on Pt(111). *J. Chem. Phys.* **2016**, *144*, 184709.

(112) Kresse, G.; Furthmüller, J. Efficient Iterative Schemes for *Ab Initio* Total-Energy Calculations Using a Plane-Wave Basis Set. *Phys. Rev. B* **1996**, *54*, 11169–11186.

(113) Kresse, G.; Furthmüller, J. Efficiency of Ab-Initio Total Energy Calculations for Metals and Semiconductors Using a Plane-Wave Basis Set. *Comput. Mater. Sci.* **1996**, *6*, 15–50.

(114) Henkelman, G.; Uberuaga, B. P.; Jónsson, H. A Climbing Image Nudged Elastic Band Method for Finding Saddle Points and Minimum Energy Paths. *J. Chem. Phys.* **2000**, *113*, 9901–9904.

(115) Henkelman, G.; Jónsson, H. Improved Tangent Estimate in the Nudged Elastic Band Method for Finding Minimum Energy Paths and Saddle Points. *J. Chem. Phys.* **2000**, *113*, 9978–9985.

(116) Tiwari, A. K.; Nave, S.; Jackson, B. The Temperature Dependence of Methane Dissociation on Ni(111) and Pt(111): Mixed Quantum-Classical Studies of the Lattice Response. *J. Chem. Phys.* **2010**, *132*, 134702.

(117) Stegelmann, C.; Andreasen, A.; Campbell, C. T. Degree of Rate Control: How Much the Energies of Intermediates and Transition States Control Rates. *J. Am. Chem. Soc.* **2009**, *131*, 8077–8082.

(118) Wellendorff, J.; Silbaugh, T. L.; Garcia-Pintos, D.; Nørskov, J. K.; Bligaard, T.; Studt, F.; Campbell, C. T. A Benchmark Database for Adsorption Bond Energies to Transition Metal Surfaces and Comparison to Selected DFT Functionals. *Surf. Sci.* **2015**, *640*, 36–44.

(119) Silbaugh, T. L.; Campbell, C. T. Energies of Formation Reactions Measured for Adsorbates on Late Transition Metal Surfaces. *J. Phys. Chem. C* **2016**, *120*, 25161–25172.

(120) Calle-Vallejo, F.; Tymoczko, J.; Colic, V.; Vu, Q. H.; Pohl, M. D.; Morgenstern, K.; Loffreda, D.; Sautet, P.; Schuhmann, W.; Bandarenka, A. S. Finding Optimal Surface Sites

on Heterogeneous Catalysts by Counting Nearest Neighbors. *Science* **2015**, *350*, 185–189.

(121) Calle-Vallejo, F.; Loffreda, D.; Koper, M. T. M.; Sautet, P. Introducing Structural Sensitivity into Adsorption-Energy Scaling Relations by Means of Coordination Numbers. *Nat. Chem.* **2015**, *7*, 403–410.

(122) Calle-Vallejo, F.; Pohl, M. D.; Reinisch, D.; Loffreda, D.; Sautet, P.; Bandarenka, A. S. Why Conclusions from Platinum Model Surfaces Do Not Necessarily Lead to Enhanced Nanoparticle Catalysts for the Oxygen Reduction Reaction. *Chem. Sci.* **2017**, *8*, 2283–2289.

(123) van Santen, R. A. Complementary Structure Sensitive and Insensitive Catalytic Relationships. *Accounts. Chem. Res.* **2009**, *42*, 57–66.

(124) Sabbe, M. K.; Reyniers, M.-F.; Reuter, K. First-Principles Kinetic Modeling in Heterogeneous Catalysis: An Industrial Perspective on Best-Practice, Gaps and Needs. *Catal. Sci. Technol.* **2012**, *2*, 2010–2024.

(125) Medford, A. J.; Vojvodic, A.; Hummelshøj, J. S.; Voss, J.; Abild-Pedersen, F.; Studt, F.; Bligaard, T.; Nilsson, A.; Nørskov, J. K. From the Sabatier Principle to a Predictive Theory of Transition-Metal Heterogeneous Catalysis. *J. Catal.* **2015**, *328*, 36–42.

(126) Latimer, A. A.; Kulkarni, A. R.; Aljama, H.; Montoya, J. H.; Yoo, J. S.; Tsai, C.; Abild-Pedersen, F.; Studt, F.; Nørskov, J. K. Understanding Trends in C–H Bond Activation in Heterogeneous Catalysis. *Nat. Mater.* **2017**, *16*, 225–229.

(127) Honkala, K.; Hellman, A.; Remediakis, I. N.; Logadottir, A.; Carlsson, A.; Dahl, S.; Christenen, C.; Nørskov, J. K. Ammonia Synthesis from First-Principles Calculations. *Science* **2005**, *307*, 555–558.

(128) Reuter, K.; Plaisance, C. P.; Oberhofer, H.; Andersen, M. Perspective: On the Active Site Model in Computational Catalyst Screening. *J. Chem. Phys.* **2017**, *146*, 040901.

(129) Plessow, P. N.; Abild-Pedersen, F. Examining the Linearity of Transition State Scaling Relations. *J. Phys. Chem. C* **2015**, *119*, 10448–10453.

(130) Weststrate, C. J.; van Helden, P.; Niemantsverdriet, J. W. Reflections on the Fischer-Tropsch Synthesis: Mechanistic Issues from a Surface Science Perspective. *Catal. Today* **2016**, *275*, 100–110.

(131) Nørskov, J. K.; Bligaard, T.; Hvolbæk, B.; Abild-Pedersen, F.; Chorkendorff, I.; Christensen, C. H. The Nature of the Active Site in Heterogeneous Metal Catalysis. *Chem. Soc. Rev.* **2008**, *37*, 2163-2171.

(132) Wei, J.; Iglesia, E. Mechanism and Site Requirements for Activation and Chemical Conversion of Methane on Supported Pt Clusters and Turnover Rate Comparisons among Noble Metals. *J. Phys. Chem. B* **2004**, *108*, 4094–4103.

(133) Xu, Y.; Lausche, A. C.; Wang, S.; Khan, T. S.; Abild-Pedersen, F.; Studt, F.; Nørskov, J. K.; Bligaard, T. *In Silico* Search for Novel Methane Steam Reforming Catalysts. *New J. Phys.* **2013**, *15*, 125021.

(134) Nakamura, J.; Campbell, J. M.; Campbell, C. T. Kinetics and Mechanism of the Water-Gas Shift Reaction Catalysed by the Clean and Cs-Promoted Cu(110) Surface: A Comparison with Cu(111). *J. Chem. Soc. Faraday T.* **1990**, *86*, 2725-2734.

(135) Campbell, C. T. Future Directions and Industrial Perspectives Micro- and Macro-Kinetics: Their Relationship in Heterogeneous Catalysis. *Top. Catal.* **1994**, *1*, 353–366.

(136) van Santen, R. A.; Markvoort, A. J.; Filot, I. A. W.; Ghouri, M. M.; Hensen, E. J. M. Mechanism and Microkinetics of the Fischer–Tropsch Reaction. *Phys. Chem. Chem. Phys.* **2013**, *15*, 17038–17063.

(137) Okeson, T. J.; Keyvanloo, K.; Lawson, J. S.; Argyle, M. D.; Hecker, W. C. On the Kinetics

and Mechanism of Fischer-Tropsch Synthesis on a Highly Active Iron Catalyst Supported on Silica-Stabilized Alumina. *Catal. Today* **2016**, *261*, 67–74.

(138) Freund, H.-J.; Nilius, N.; Risse, T.; Schauermann, S. A Fresh Look at an Old Nano-Technology: Catalysis. *Phys. Chem. Chem. Phys.* **2014**, *16*, 8148-8167.

(139) Ceyer, S. T.; Yang, Q. Y.; Lee, M. B.; Beckerle, J. D.; Johnson, A. D. The Mechanism for the Dissociation of Methane on a Nickel Catalyst. *Stud. Surf. Sci. Catal.* **1988**, *36*, 51–66.

(140) Beckerle, J. D.; Johnson, A. D.; Yang, Q. Y.; Ceyer, S. T. Collision Induced Dissociative Chemisorption of $CH_4$ on Ni(111) by Inert Gas Atoms: The Mechanism for Chemistry with a Hammer. *J. Chem. Phys.* **1989**, *91*, 5756–5777.